Transverse-rapidity y_t dependence of the nonjet azimuth quadrupole from 62- and 200-GeV Au-Au collisions

David T. Kettler, Duncan J. Prindle, and Thomas A. Trainor
CENPA 354290, University of Washington, Seattle, Washington 98195, USA
(Received 10 April 2015; published 29 June 2015)

Previous measurements of a quadrupole component of azimuth correlations denoted by symbol v_2 have been interpreted to represent elliptic flow, a hydrodynamic phenomenon conjectured to play a major role in noncentral nucleus-nucleus collisions. v_2 measurements provide the main support for conclusions that a "perfect liquid" is formed in heavy-ion collisions at the Relativistic Heavy Ion Collider. However, conventional v_2 methods based on one-dimensional (1D) azimuth correlations give inconsistent results and may include a jet contribution. In some cases the data trends appear to be inconsistent with hydrodynamic interpretations. In this study we distinguish several components of 2D angular correlations and isolate a *nonjet* (NJ) azimuth quadrupole denoted by $v_2\{2D\}$. We establish systematic variations of the NJ quadrupole on y_t, centrality, and collision energy. We adopt transverse-rapidity y_t as both a velocity measure and a logarithmic alternative to transverse momentum p_t. Based on NJ-quadrupole trends, we derive a completely factorized universal parametrization of quantity $v_2\{2D\}(y_t, b, \sqrt{s_{NN}})$ which describes the centrality, y_t, and energy dependence. From y_t-differential $v_2(y_t)$ data we isolate a *quadrupole spectrum* and infer a *quadrupole source boost* having unexpected properties. NJ quadrupole v_2 trends obtained with 2D model fits are remarkably simple. The centrality trend appears to be uncorrelated with a *sharp transition* in jet-related structure that may indicate rapid change of Au-Au medium properties. The lack of correspondence suggests that the NJ quadrupole may be insensitive to such a medium. Several quadrupole trends have interesting implications for hydro interpretations.

DOI: 10.1103/PhysRevC.91.064910 PACS number(s): 25.75.Ag, 25.75.Bh, 25.75.Ld, 25.75.Nq

I. INTRODUCTION

Measurements of the quadrupole component of azimuth ϕ correlations from Relativistic Heavy Ion Collider (RHIC) heavy-ion collisions in the form $v_2 = \langle \cos(2\phi) \rangle$ relative to estimates of the A-A reaction-plane angle are conventionally interpreted to represent *elliptic flow*, a conjectured hydrodynamic response to pressure gradients in the initial collision system corresponding to the overlap eccentricity of colliding nuclei [1]. In a hydrodynamic (hydro) context [2–4] inferred large elliptic flow values combined with other measurements are interpreted to imply rapid thermalization and production of a QCD medium with large energy density and small viscosity described as a "perfect liquid" [5–7].

However, questions persist concerning v_2 measurements and interpretations. Conventional one-dimensional (1D) v_2 methods [8,9] may not distinguish accurately between a *nonjet* (NJ) azimuth quadrupole (*cylindrical multipole* uniform on pseudorapidity η over a significant interval near midrapidity) and certain jet-related angular correlations that vary strongly with η near midrapidity [10–13]. The terms jet-related and nonjet are discussed in Sec. II B.

In previous studies we introduced a physical-model-independent method to distinguish *geometrically* between a NJ quadrupole and the quadrupole ($m = 2$) Fourier component of jet-related angular correlations dominated by a 2D peak centered at the origin on η and ϕ difference variables [14,15]. The notation $v_2\{2D\}$ distinguishes the quadrupole component derived from model fits to 2D histograms from $v_2\{\text{method}\}$ data inferred with conventional 1D methods. We observed that p_t-integral $v_2\{2D\}(b, \sqrt{s_{NN}})$ data follow simple trends described by a few parameters over a broad range of centrality and collision energy $\sqrt{s_{NN}}$ above 13 GeV. The trends factorize, each factor described by a simple function. That analysis was complementary to an analysis reported in Ref. [16] focusing on jet-related structure.

In the present study we extend the NJ-quadrupole program to measurements of y_t-differential $v_2\{2D\}(y_t, b, \sqrt{s_{NN}})$ also derived from 2D model fits. As an alternative to transverse momentum p_t, we introduce transverse-rapidity y_t as a logarithmic variable (defined below) compatible with relativistic boost measurements. From y_t-differential $v_2\{2D\}$ data it is possible to infer a *quadrupole source boost* distribution common to hadrons of several species [17,18]. In this study we determine the Au-Au centrality dependence of the quadrupole source boost. We also infer a corresponding *quadrupole spectrum* common to several hadron species [18] and substantially different from the spectrum for most final-state hadrons. Those results offer new insights into possible mechanisms for the NJ azimuth quadrupole.

This paper is arranged as follows. In Sec. II we introduce some general correlation analysis methods. In Secs. III and IV we describe two alternative methods for estimating azimuth quadrupole components of angular correlations. In Sec. V we introduce measured y_t-differential 2D angular autocorrelations (histograms) derived from particle data. In Sec. VI we review systematic model-parameter trends from model fits to the 2D data histograms. In Sec. VII we define the quadrupole source boost and determine its centrality dependence. In Sec. VIII we extract quadrupole spectra and describe the centrality dependence. In Sec. IX we derive a universal factorized parametrization of NJ quantity $v_2\{2D\}(y_t, b, \sqrt{s_{NN}})$. In Sec. X we discuss systematic uncertainties, and in Sec. XI we present comparisons between quadrupole amplitudes derived from 2D fits to angular correlations and from other v_2 methods. In Secs. XII and XIII we present discussion and summary.

II. GENERAL ANALYSIS METHODS

In this study we report measurements of y_t-differential $V_2^2\{2D\}(y_t,b)$ NJ azimuth *power-spectrum* elements derived from model fits to 2D angular correlations. Transverse-rapidity y_t (defined below) serves as a logarithmic measure of transverse momentum p_t.

A. Kinematic measures and spaces

A-A collisions with impact parameter b produce final-state hadrons in cylindrical 3D momentum space (p_t,η,ϕ), where p_t is transverse momentum, η is pseudorapidity, and ϕ is azimuth angle. Transverse mass is $m_t = \sqrt{p_t^2 + m_h^2}$ with hadron mass m_h. Pseudorapidity is defined by $\eta = -\ln[\tan(\theta/2)]$ (θ is polar angle relative to collision axis z), and $\eta \approx \cos(\theta)$ near $\eta = 0$. Transverse rapidity is defined by $y_t = \ln[(m_t + p_t)/m_h]$. For identified hadrons the proper hadron mass is used and y_t is then a velocity measure appropriate to test flow conjectures. For unidentified hadrons y_t with pion mass assumed (about 80% of hadrons) serves as a logarithmic measure of p_t, and the pion mass regularizes the logarithmic trend for small values of p_t. The solenoidal tracker at RHIC (STAR) Time Projection Chamber (TPC) acceptance $p_t > 0.15$ GeV/c corresponds to $y_t > 1$.

Two-particle correlations are structures in the pair density on 6D momentum space $(y_{t1},\eta_1,\phi_1,y_{t2},\eta_2,\phi_2)$. Angular correlations can be measured on subspace $(\eta_1,\eta_2,\phi_1,\phi_2)$ given some conditions on transverse momentum (p_{t1},p_{t1}) or transverse-rapidity (y_{t1},y_{t2}). We can integrate over all y_t (y_t-integral analysis) or define conditions on two particles (y_{t1},y_{t2}) (y_t-differential analysis). Alternatively, we can integrate over some part of the angular acceptance (angular acceptance conditions) to study conditional correlations on (y_{t1},y_{t2}) [19–22].

An *autocorrelation* on angular subspace (x_1,x_2) is derived by averaging pair density $\rho(x_1,x_2)$ along diagonals on (x_1,x_2) parallel to the sum axis $x_\Sigma = x_1 + x_2 y$. The averaged pair density $\rho(x_\Delta)$ on defined *difference variable* $x_\Delta = x_1 - x_2$ is then an autocorrelation [23]. For correlation structure approximately independent of x_Σ over some limited acceptance Δx (stationarity, typical over 2π azimuth and within some limited pseudorapidity interval $\Delta\eta$) angular correlations remain undistorted (no information is lost in the projection by averaging) [24]. Within the STAR TPC acceptance $\Delta\eta = 2, \Delta\phi = 2\pi$ [25] 2D angular autocorrelations are lossless projections of 6D two-particle momentum space onto angle difference axes $(\eta_\Delta,\phi_\Delta)$ [26]. The ϕ_Δ axis is divided into *same-side* (SS, $|\phi_\Delta| < \pi/2$) and *away-side* (AS, $\pi/2 < |\phi_\Delta| < \pi$) regions.

In the present analysis we impose conditions on the space (y_{t1},y_{t2}) to establish the full $(y_t,b,\sqrt{s_{NN}})$ systematics of angular correlations, emphasizing the NJ quadrupole obtained from 2D model fits via two model parameters: *per-particle* quadrupole amplitude $A_Q\{2D\}$ or *per-pair* amplitude $B_Q\{2D\}$ (terms defined below).

B. Correlation structure and interpretations

The 2D data histograms that form the basis for this study (within the STAR TPC acceptance) exhibit the same three dominant features from p-p to central Au-Au collisions: (a) a SS 2D peak centered at the origin on $(\eta_\Delta,\phi_\Delta)$, (b) an AS 1D peak centered at $\phi_\Delta = \pi$ and approximately uniform on η_Δ, and (c) an azimuth quadrupole component uniform on η_Δ. Those three elements are distinguished in all cases by model fits to 2D angular correlations on η_Δ and ϕ_Δ. Component (a) is well-described by a SS 2D Gaussian in most cases. With increasing A-A centrality the SS peak is elongated on η_Δ. If high-p_t (trigger-associated) cuts are applied, the SS peak may develop non-Gaussian tails on η_Δ. Component (b) is well described by a single AS dipole term.

In p-p and more-peripheral Au-Au collisions components (a) and (b) represent intrajet and interjet correlations, respectively: Their amplitudes scale with the number of binary N-N collisions $N_{\rm bin}$ as expected for dijets, and their forms are consistent with perturbative quantum chromodynamics (pQCD) jet structure predicted by PYTHIA [27] and HIJING [28]. They both retain the same forms and follow $N_{\rm bin}$ scaling (N-N linear superposition) in Au-Au collisions up to 50% centrality [16]. Throughout that centrality interval it is therefore appropriate to refer to (a) and (b) as *jet-related* structures. In more-central Au-Au collisions (above a *sharp transition* near 50% centrality [16]) the SS 2D peak becomes increasingly elongated on η_Δ, and the peak amplitude increases faster than $N_{\rm bin}$ scaling. However, other features of the SS peak remain consistent with jet production [29]. The AS dipole amplitude closely follows the SS 2D peak amplitude and also remains consistent with jet expectations. Nevertheless, other (nonjet) interpretations have been proposed for those structures [30,31].

Azimuth quadrupole component (c) appears to be uncorrelated with jet-related components (a) and (b), for example, exhibiting a smooth centrality dependence with no evidence of the sharp transition [14,16]. In that context it is appropriate to refer to (c) as the NJ quadrupole. The NJ quadrupole inferred from 2D model fits (represented by symbol $v_2\{2D\}$) is an isolated quadrupole structure uniform on η near midrapidity with maxima at 0 and π on azimuth. Its form is then consistent with conventional expectations for "elliptic flow" if that physical mechanism is relevant. The SS 2D peak (a) projected onto 1D azimuth can be modeled as a narrow Gaussian with its own Fourier series representation [32]. The SS peak Fourier terms then contribute to any 1D Fourier description of all correlation structures combined. Resulting series terms v_m then include admixtures of elements (a), (b), and (c). In this study we show that multiple (physical) contributions to such a 1D Fourier series can be distinguished. We therefore refer to NJ quadrupole (c) as the object of the present study distinct from a jet-related quadrupole derived from (a), which may be a source of systematic error for 1D v_2 analysis [33].

C. Joint and marginal distributions on (y_{t1}, y_{t2})

This analysis addresses angular correlation systematics corresponding to various cut conditions on space (y_{t1},y_{t2}). Figure 1 (left panel) shows the relation between transverse momentum p_t and transverse-rapidity y_t. $y_t \approx 1$ ($p_t \approx 0.15$ GeV/c) is the typical lower p_t bound defining the TPC acceptance for spectra and correlations. The dotted line $(m_\pi/2)\exp(y_t) \approx p_t$ demonstrates that y_t accurately represents $\log(p_t)$ over the TPC p_t acceptance. The close

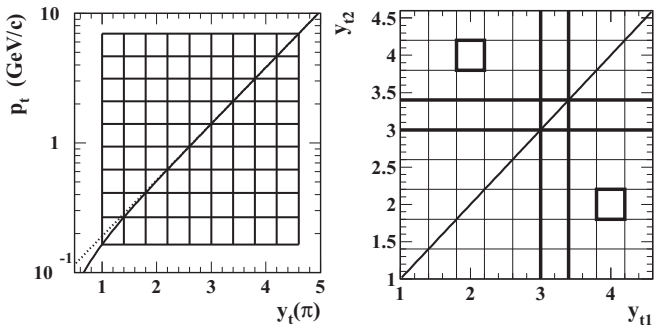

FIG. 1. (Left) The relation between transverse momentum p_t and transverse-rapidity $y_t(\pi)$ (assuming a pion mass). The grid shows the uniform y_t bin system used for the present analysis. The dotted line provides a $\log(p_t)$ reference for comparison. (Right) The symmetrized two-particle space (y_{t1}, y_{t2}). An element of the *joint* distribution on (y_{t1}, y_{t2}) is shown by the bold squares. An element of the *marginal* distribution on y_t is shown by the bold rectangles.

correspondence down to the p_t acceptance limit arises because the pion mass is ≈ 0.1 GeV/c. The grid illustrates the cut system for this analysis, nine bins on y_t with fixed width $\delta y_t = 0.4$. The p_t interval covered by the analysis is [0.16,7] GeV/c.

Figure 1 (right panel) shows the binning on (y_{t1}, y_{t2}) for the y_t-differential analysis. The binning system is symmetric about the diagonal. The bold squares illustrate an element of the *joint* distribution on (y_{t1}, y_{t2}). By integrating over one axis we obtain the 1D projection or *marginal* distribution on y_t represented by the bold rectangles. The marginal format is the basis for the y_t-differential part of this analysis. Because the cut system (equal y_t bins) and other aspects of this analysis are based on y_t, we prefer that quantity in the text, with occasional references to specific p_t values.

D. Single-particle and correlated-pair measures

The single-charged-particle (SP) y_t spectrum is $\rho_0(y_t,b) = d^2n_{\rm ch}/y_t dy_t 2\pi d\eta$ (azimuth averaged). The y_t-integral angular density is $\rho_0(b) = \int dy_t\, y_t \rho_0(y_t,b) \approx n_{\rm ch}/2\pi\Delta\eta$ averaged over acceptance $\Delta\eta$. The two-component particle-yield parametrization [34], as applied in this analysis, is $\rho_0(b) = \rho_{pp}(N_{\rm part}/2)[1 + x(\nu - 1)]$, where $2\pi\rho_{pp}$ and x are 2.5 and 0.095, respectively, for more-central 200-GeV Au-Au collisions. Glauber-model centrality parameters $N_{\rm part}/2$ and ν are defined below.

$\rho(\vec{p}_1, \vec{p}_2)$ is the basic pair density on 6D pair momentum space. The event-averaged pair density $\rho_{\rm sib}$ derived from sibling pairs (pairs drawn from single events) includes the correlation structures to be measured. $\rho_{\rm mix}$ is the density of mixed pairs drawn from different but similar events. $\rho_{\rm ref}$ denotes a minimally correlated reference-pair density derived from (a) a mixed-pair density or (b) a product of SP densities via a factorization assumption. On pair subspace (y_{t1}, y_{t2}) the factorized joint reference is $\rho_{\rm ref}(y_{t1}, y_{t2}, b) = \rho_0(y_{t1}, b)\rho_0(y_{t2}, b)$, the marginal reference is $\rho_{\rm ref}(y_t, b) = \rho_0(b)\rho_0(y_t, b)$, and the y_t-integral reference is $\rho_{\rm ref}(b) = \rho_0^2(b)$.

Formation of autocorrelation histograms on difference variables $(\eta_\Delta, \phi_\Delta)$ projected from pair angle subspace $(\eta_1, \phi_1, \eta_2, \phi_2)$ has been described previously [16,23]. Pair histograms so formed are approximately uniform on η_Δ and ϕ_Δ. Small deviations from uniformity represent correlations of interest. Pair histograms formed by simple projection from (η_1, η_2) (not autocorrelations) include a triangular pair acceptance on difference variable η_Δ.

Differential correlation structure is determined by comparing a sibling-pair density to a reference-pair density in the form of difference $\Delta\rho = \rho_{\rm sib} - \rho_{\rm ref}$ representing a correlated-pair density or *covariance* density. There are then two choices for a *relative* correlation measure.

(a) *Per-particle* measure $\Delta\rho/\sqrt{\rho_{\rm ref}}$ has the form of Pearson's normalized covariance wherein the numerator is a covariance and the denominator is the geometric mean of marginal variances. In the Poisson limit a marginal variance is given by $\sigma_n^2 = \bar{n} \propto \rho_0$. Because $\rho_{\rm ref} \approx \rho_0 \times \rho_0$ it follows that the geometric mean of variances is given by $\sqrt{\rho_{\rm ref}} \propto n_{\rm ch}$ and the normalized covariance is a per-particle correlation measure [11,12,23].

(b) *Per-pair* measure $\Delta\rho/\rho_{\rm ref}$ *decreases* trivially with system size as $1/n_{\rm ch}$. That trend obscures smaller but physically meaningful variations. The per-pair measure also tends to *increase* trivially as a function of y_t because the pair ratio includes the SP spectrum in its denominator. The dominant SP spectrum trend also obscures physically meaningful correlation variations.

In a practical correlation analysis pair ratio $\Delta\rho/\rho_{\rm ref} \to \Delta\rho/\rho_{\rm mix}$ is first calculated directly to cancel particle-pair detector inefficiencies. The per-particle measure $\Delta\rho/\sqrt{\rho_{\rm ref}} \equiv \sqrt{\rho_{\rm ref}}\Delta\rho/\rho_{\rm mix}$ is then obtained, where $\rho_{\rm ref}$ is constructed from *corrected* SP spectra $\rho_0(y_t, b)$ and yields $\rho_0(b)$ [16].

In this y_t-differential analysis we present per-pair quadrupole measurements based on 2D model fits to angular correlations. The basic measures are the Fourier components V_m^2 of $\Delta\rho(\phi_\Delta)$ emphasizing the quadrupole term V_2^2. The per-pair ratio $\Delta\rho/\rho_{\rm mix}$ gives $B_Q\{2{\rm D}\}(y_t, b) = v_2^2\{2{\rm D}\}(y_t, b)$ directly comparable with published $v_2(p_t)$ data. The per-particle measure $\sqrt{\rho_{\rm ref}}\Delta\rho/\rho_{\rm mix}$ gives $A_Q\{2{\rm D}\}(b) = \rho_0(b)v_2^2\{2{\rm D}\}(b)$ exhibiting simple systematic trends on centrality and collision energy [14,15]. Because $V_2^2(y_t, b) = \rho_0(b)\rho_0(y_t, b)(b)v_2^2(y_t, b)$, we have $\rho_0(b)A_Q(b) = V_2^2(b)$ and $\rho_0(b)\rho_0(y_t, b)B_Q(y_t, b) = V_2^2(y_t, b)$, defining per-particle $A_Q(b)$ and per-pair $B_Q(y_t, b)$ quadrupole measures. Per-particle and per-pair measures are thus exactly related. For reasons noted above, V_2^2 and per-particle measure A_Q are the bases for physical interpretations. The per-pair measure B_Q from this y_t-differential study does not require corrected SP spectra $\rho_0(y_t, b)$ and provides direct comparison with published $v_2(p_t)$ data.

E. *A-A* centrality measures

A-A centrality is measured by matching the fractional cross section σ/σ_0 for some observed $n_{\rm ch}$ to the fractional cross section derived from a Glauber Monte Carlo simulation. Glauber parameters $N_{\rm part}/2$ (participant pairs) and $N_{\rm bin}$ (*N-N* binary collisions) and impact parameter b are thereby related to $n_{\rm ch}$ integrated within the TPC acceptance $|\eta| < 1$. The fractional impact parameter is defined by $b/b_0 \equiv \sqrt{\sigma/\sigma_0}$. Centrality measure $\nu \equiv 2\, N_{\rm bin}/N_{\rm part}$ estimates the mean number of *N-N* encounters per participant nucleon (mean projectile-nucleon path length across the collision-partner nucleus). We use the

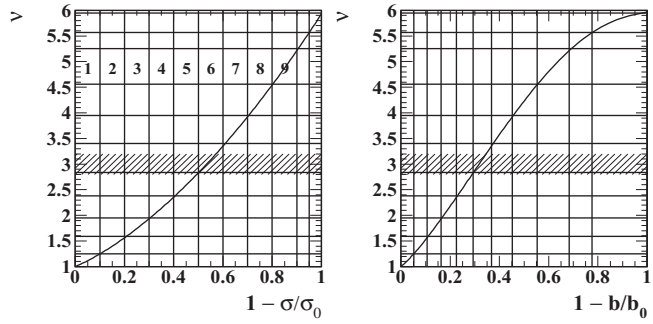

FIG. 2. (Left) Mean participant path length ν vs fractional cross-section measure $1-\sigma/\sigma_0$. The grid shows the 11 centrality bins for this analysis. The hatched region indicates the "sharp transition" in jet-related correlation properties reported in Ref. [16]. (Right) Path length ν vs fractional impact parameter $b/b_0 = \sqrt{\sigma/\sigma_0}$. For Au-Au collisions $b_0 \approx 14.7$ fm.

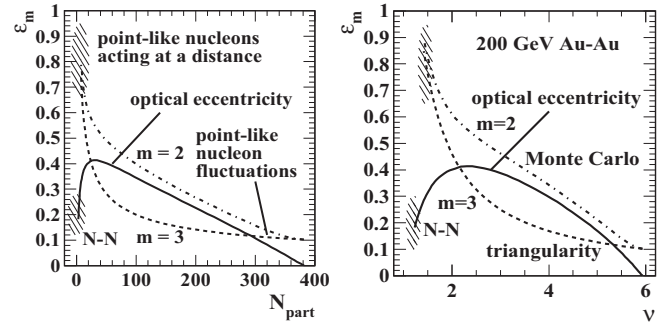

FIG. 3. Centrality trends for optical and Monte Carlo Glauber IS azimuth multipoles with $m = 2, 3$ on participant-projectile-nucleon number (left panel) and binary N-N collisions ν per participant-nucleon pair (right panel).

same Glauber parameters for all energies as purely geometrical measures (the 200 GeV N-N cross section $\sigma_{NN} = 42$ mb is assumed for all cases).

Figure 2 (left panel) shows participant path length ν vs fractional cross section in the form $1-\sigma/\sigma_0$ inferred from a Glauber Monte Carlo. The hatched band, with position inferred from angular correlation data, represents a *sharp transition* in jet-related correlation systematics, below which jet correlations follow the N-N binary-collision scaling expected for linear superposition of N-N collisions (A-A transparency) and no jet modification [16]. Figure 2 (right panel) shows ν vs fractional impact parameter as $1-b/b_0$, where $b_0 \approx 14.7$ fm for Au-Au collisions.

The grids in Fig. 2 indicate the centrality bins for this analysis defined as follows. Uncorrected minimum-bias event samples are divided into 11 nominal centrality bins: $9 \approx 10\%$ bins from 100% to 10%, the last 10% divided into 2 5% bins. The corrected centrality of each bin as modified by tracking and event vertex inefficiencies is determined by a running-integral procedure described in Ref. [35]. Centralities from N-N collisions ($\nu \approx 1.25$) to central A-A ($b \approx 0$) are thereby determined to 2%.

F. *A-A* initial-state geometry measures

Some features of the initial-state (IS) geometry of A-A collisions may influence collision dynamics. Initial-state azimuth structure is conventionally modeled by a Glauber Monte Carlo. The participant-nucleon azimuth distribution can be described by an autocorrelation function on azimuth difference ϕ_Δ [23]. For noncentral A-A collisions the autocorrelation includes (a) a few even-m sinusoids dominated by $m = 2$ (IS quadrupole) phase-correlated with vector impact parameter $\vec{b}$ (the eccentric A-A overlap region), (b) a uniform background, and (c) a δ-function term $\propto N_{\rm part}$ (self pairs) uncorrelated with $\vec{b}$.

The Fourier transform of the IS azimuth autocorrelation is a power spectrum represented by eccentricity elements $E_m^2 = N_{\rm part}^2 \epsilon_m^2$, with *per-pair* eccentricity measures [33]

$$\epsilon_{m,\rm MC}^2 = \epsilon_{m,opt}^2 + \sigma_{\epsilon_m}^2 + \delta\epsilon_m^2 \text{ for } m \text{ even}$$
$$= \delta\epsilon_m^2 \text{ for } m \text{ odd}, \quad (1)$$

where $\sigma_{\epsilon_m}^2$ represents an eccentricity variance owing to eventwise b fluctuations. Eccentricities $\epsilon_{m,\rm opt}^2$ ($m = 2,\ 4$) represent the "elliptical" A-A overlap region for fixed b and smooth matter distributions. The corresponding $m = 2$ optical eccentricity for 200-GeV Au-Au is parametrized by [15]

$$\epsilon_{2,\rm opt} = \frac{1}{5.4}\left[\log_{10}\left(\frac{3\,N_{\rm bin}}{2}\right)\right]^{0.96}\left[\log_{10}\left(\frac{1136}{N_{\rm bin}}\right)\right]^{0.78}. \quad (2)$$

Pointwise Monte Carlo random sampling generates a "white-noise" power spectrum $\delta\epsilon_m^2 \propto 1/N_{\rm part}$ (approximately uniform on m) corresponding to the self-pair contribution $\approx N_{\rm part}\delta(\phi_\Delta)$ in the IS azimuth autocorrelation. For a stochastic process there should be no phase relation between noise amplitudes $\delta\epsilon_m^2$ and impact parameter $\vec{b}$. All higher m are present in the IS Monte Carlo spectrum and *might* appear in the observed final state to some extent *if* Monte Carlo sampling at $x \approx 1/3$ were a legitimate model of IS geometry relevant to FS hadron production for $\eta \approx 0$ and $x \approx 0.01$.

Figure 3 shows centrality trends for $m = 2,\ 3$ IS power-spectrum elements on participant-nucleon number $N_{\rm part}$ (left panel) and mean participant path length ν (right panel). Plotted are optical eccentricity $\epsilon_{2,\rm opt}$ (solid curves), Monte Carlo eccentricity $\epsilon_{2,\rm MC}$ (dash-dotted curves), and so-called "triangularity" $\delta\epsilon_3$ (dashed curves). From Eq. (1) (and ignoring a possible $\sigma_{\epsilon_2}^2$ contribution) we have $\epsilon_{2,\rm MC}^2 = \epsilon_{2,\rm opt}^2 + \delta\epsilon_2^2$, with $\delta\epsilon_2^2 \approx 4/N_{\rm part}$ and $\epsilon_{3,\rm MC}^2 = \delta\epsilon_3^2 \approx 4/N_{\rm part}$.

Whether point-like-nucleon sampling at nucleon momentum fraction $x \approx 1/3$ represents an IS geometry with significant manifestations in FS correlation structure for $x \approx 0.01$ is an open question. The present analysis indicates that optical eccentricity $\epsilon_{2,\rm opt}$ is most compatible with NJ $v_2\{2D\}$ data obtained from 2D model fits.

III. NONGRAPHICAL NUMERICAL METHODS

In this section we present a simplified analysis method confined to 1D azimuth difference ϕ_Δ corresponding to projection $\rho(\eta_\Delta,\phi_\Delta) \to \rho(\phi_\Delta)$ of all 2D angular correlation structure within some detector η acceptance $\Delta\eta$. This description is directly related to conventional 1D v_2 analysis via *nongraphical numerical methods* (NGNMs). In Sec. IV

we describe a more-general analysis method based on model fits to 2D data histograms on $(\eta_\Delta,\phi_\Delta)$, the basis for the present NJ-quadrupole study.

A. Pair densities on azimuth difference ϕ_Δ

$\rho(\phi_\Delta)$ is the (4D angular) pair-density projection onto azimuth difference ϕ_Δ obtained by *averaging* over η_Δ within acceptance $\Delta\eta$. Any distribution on periodic ϕ_Δ can be described exactly by a Fourier series,

$$\rho(\phi_\Delta) = \frac{1}{2\pi\,\Delta\eta^2}\overline{\sum_{i,j=1,\in\Delta\eta}^{n}\delta(\phi_i-\phi_j-\phi_\Delta)} = \delta(\phi_\Delta)\rho_0/\Delta\eta + V_0^2 + 2\sum_{m=1}^{\infty}V_m^2\cos(m\phi_\Delta), \quad (3)$$

with $V_m^2 \equiv V_0^2 v_m^2$ and $V_0^2 = \overline{n(n-1)}/(2\pi\,\Delta\eta)^2$ (overline indicates event-ensemble average). The sum upper limit is simplified by $n_{\rm ch}\to n$. That expression describes all pairs within the angular acceptance including self-pairs $i=j$. The Fourier coefficients V_m^2 constitute the *power spectrum* of the azimuth pair density [36]. Any and all significant correlation structure *projected onto azimuth* should be accurately represented by the V_m^2, which are additive or extensive measures (whereas the v_m^2 are not). The δ function on the right-hand side represents self pairs ($i=j$) and has its own Fourier series representation (a uniform or "white-noise" power spectrum on m) [36].

In this analysis we consider the azimuth quadrupole (a cylindrical multipole) term of the power spectrum. The $m=2$ Fourier coefficient (also a 4D angular density) with *self-pairs excluded* is determined from data by

$$V_2^2(b) = \frac{1}{2\pi}\int_0^{2\pi}d\phi_\Delta\rho(\phi_\Delta,b)\cos(2\phi_\Delta) = \frac{1}{(2\pi\,\Delta\eta)^2}\overline{\sum_{i\neq j=1,\in\Delta\eta}^{n,n-1}\langle\cos[2(\phi_i-\phi_j)]\rangle} \equiv \rho_0^2(b)v_2^2(b) \approx \rho_0^2(b)\langle\cos(2\phi_\Delta)\rangle. \quad (4)$$

The approximation in the last line is for $n\gg 1$. For conventional notation $v_2\{\text{method}\}$, Eq. (4) represents $V_2^2\{2\}$ derived from two-particle 1D azimuth correlations. Recent "higher-harmonic" Fourier analysis extends to $m>2$, interpreting any v_m as representing a flow [30]. Equation (4) is actually equivalent to a model fit to 2D angular correlations projected onto 1D azimuth. Model-fit comparisons are discussed further in Sec. IV.

B. y_t-differential $V_2^2\{2\}(y_t,b)$ measurement

Figure 1 (right panel) shows joint and marginal conditions on (y_{t1},y_{t2}) (bold lines). The *joint* distribution (6D density) on (y_{t1},y_{t2}) is defined by

$$V_2^2(y_{t1},y_{t2},b) = \frac{1}{(\delta y_t 2\pi\,\Delta\eta)^2}\overline{\sum_{i\in y_{t1}\neq j\in y_{t2}}^{n_{y_{t1}},n_{y_{t2}}}\frac{\cos[2(\phi_i-\phi_j)]}{y_{t1}y_{t2}}}, \quad (5)$$

where $\delta y_t = 0.4$ is the bin width on y_t (uniform widths in this analysis). The *marginal* distribution is defined by

$$V_2^2(y_t,b) = \frac{1}{2\pi}\int_0^{2\pi}d\phi_\Delta\rho(y_t,\phi_\Delta,b)\cos(2\phi_\Delta) = \frac{1}{\delta y_t(2\pi\,\Delta\eta)^2}\overline{\sum_{i\in y_t\neq j=1}^{n_{y_t},n-1}\frac{\cos[2(\phi_i-\phi_j)]}{y_t}} = \int_0^\infty dy_t' y_t' V_2^2(y_t,y_t',b) \equiv V_2(b)V_2(y_t,b) = \rho_0(b)\rho_0(y_t,b)v_2^2(y_t,b), \quad (6)$$

where $\rho_0(y_t,b)$ is the SP spectrum on y_t. $V_2(y_t,b)\equiv V_2^2(y_t,b)/V_2(b)$ with $V_2(b)\equiv\sqrt{V_2^2(b)}$ defines a self-consistent extensive measure system.

In some conventional NGNM v_2 analyses the pair ratio is calculated directly as the ensemble mean of a ratio,

$$v_2^2(y_t,b) = \overline{\frac{1}{n_{y_t}(n-1)}\sum_{i\in y_t\neq j=1}^{n_{y_t},n-1}\cos[2(\phi_i-\phi_j)]} \equiv v_2(b)v_2(y_t,b), \quad (7)$$

whereas in other analyses a ratio of mean values is employed. The pair ratio does cancel detector imperfections to some extent. Quadrupole amplitudes $V_2^2(y_t,b)$ can be approximated by using corrected y_t spectra $\rho_0(y_t,b)$ and angular densities $\rho_0(b)$ averaged over 2π and some η acceptance $\Delta\eta$ (e.g., STAR TPC). Data from NGNM applied to two-particle correlations are denoted by $v_2\{2\}$. The $v_2\{2\text{D}\}$ method used in the present study and based on model fits to 2D angular correlations is described next.

IV. MODEL FITS TO 2D (η,ϕ) CORRELATIONS

In this section we extend NGNM analysis of 1D azimuth projections to *graphical* analysis of 2D angular autocorrelations via fits to data with a 2D model function including several elements. The η dependence of angular correlations is used to distinguish among several functional forms that are later interpreted physically by comparisons with theory predictions. A *per-particle* model appropriate for studying Glauber linear superposition in the context of jet production [16] with amplitudes denoted by quantities A_X was applied in a previous y_t-integral $v_2\{2\text{D}\}$ analysis [14,15]. A *per-pair* model with amplitudes denoted by B_X is applied in the present y_t-differential analysis to provide direct comparison with $v_2(p_t)$ data from conventional 1D analysis. The B_x format does not require corrected SP spectra $\rho_0(y_t,b)$.

A. Motivation for 2D model fits

Nongraphical numerical method data (e.g., $v_2\{2\}$) derived from 1D projections discard the η structure of 2D angular correlations. Although a Fourier series can represent accurately any 1D azimuth distribution, multiple physical mechanisms may then contribute to any single Fourier amplitude (azimuth multipole) [37]. One-dimensional Fourier analysis may be

unsuited to describe 2D angular correlations from p-p and peripheral A-A collisions, which include strong variations on η_Δ accurately described by a combination of 1D and 2D peaked functions [21,22]. In that case a 1D Fourier series cannot describe angular correlations comprehensively over all A-A centralities as required to understand the centrality evolution of collision phenomena [32].

A 2D data model composed of elementary functions can remove ambiguities arising from 1D projection onto azimuth. The basic premise is as follows: Within some limited η acceptance, 2D structure is separated into what is approximately uniform on η and what is strongly varying. The nearly-uniform components are *candidates* for 1D Fourier representation. However, alternative representations (e.g., 1D Gaussian on azimuth) are also considered. Any components nonuniform on η should be modeled by the simplest combination of elementary functions *sufficient* to describe the 2D data accurately.

B. Isolating and modeling 2D correlation structure

If Eq. (3) is evaluated for particle pairs drawn from the same event the result is the sibling-pair density $\rho_{\rm sib}$. If pairs are drawn from different but similar events, the resulting mixed-pair density $\rho_{\rm mix}$ is approximately equal to the factorized reference density $\rho_{\rm ref} = V_{0,\rm ref}^2 = \rho_0^2$. In that context the density of "correlated pairs" (a covariance density *with self-pairs excluded*) is

$$\Delta\rho(\phi_\Delta) = \rho_{\rm sib} - \rho_{\rm ref} = \Delta V_0^2 + 2\sum_{m=1}^{\infty} V_m^2 \cos(m\phi_\Delta), \quad (8)$$

and the per-pair measure of correlated pairs is pair ratio

$$\frac{\Delta\rho}{\rho_{\rm ref}} = \Delta v_0^2 + 2\sum_{m=1}^{\infty} v_m^2 \cos(m\phi_\Delta). \quad (9)$$

Note that v_1^2 in that series represents a *cylindrical* multipole, not the *spherical* multipole associated with "directed flow" v_1 [9]. The quantity $\Delta V_0^2 = V_0^2 - V_{0,\rm ref}^2$ is proportional to fluctuation measure $\sigma_n^2 - \bar{n}$ (variance difference) representing number angular correlations with characteristic lengths comparable to or exceeding the acceptance scale [11,23]. We wish to extend the mathematical representation of Eq. (8) to 2D angular correlations.

In all 2D data histograms we observe an AS structure (AS ridge) that is broad on azimuth and *approximately uniform on* η_Δ within the TPC angular acceptance. The latter property implies that the AS structure is a candidate for 1D Fourier representation, but the former property implies that only a few terms in the Fourier series of Eq. (8) are required by the data, and two terms (dipole and quadrupole) are sufficient in most cases. An $m = 1$ AS dipole is generally consistent with pQCD jet structure in minimum-bias angular correlations, and the $m = 2$ NJ quadrupole is the object of the present study.

The remaining 2D structure is strongly varying on η_Δ and therefore not suitable for 1D Fourier series representation. The η-dependent 2D structure is represented by a *non-Fourier* (NF) term. The model function is then

$$\Delta\rho(\eta_\Delta,\phi_\Delta) \equiv \Delta\rho_{\rm NF}(\eta_\Delta,\phi_\Delta) + 2\sum_{m=1}^{2} V_m^2 \cos(m\phi_\Delta), \quad (10)$$

where $\Delta\rho_{\rm NF}$ is a combination of 1D (on η_Δ) and 2D peaked functions plus constant offset.

In p-p collisions the NF contribution dominates 2D angular correlations and consists of elements predominantly associated with either like-sign charge pairs or unlike-sign pairs (whereas the NJ quadrupole is observed to include both types equally) [21,22]. NF includes a 1D peak on η_Δ nearly uniform on ϕ_Δ and a complex SS 2D peaked structure at the $(\eta_\Delta,\phi_\Delta)$ origin. Most of the SS 2D peak can be modeled by a 2D Gaussian consistent in its properties with pQCD jet expectations [29]. A smaller 2D *exponential* contribution is consistent with Bose-Einstein correlations (BECs) plus conversion-electron pairs [16].

In more-central Au-Au collisions the minimum-bias SS 2D peak becomes elongated on η_Δ and slightly narrower on ϕ_Δ compared to p-p collisions but remains statistically consistent with a 2D Gaussian [16]. A NJ quadrupole is visually obvious in more-central Au-Au data [10,16], but the quadrupole component remains statistically significant for all Au-Au centralities down to N-N collisions [15]. Thus, parametric evolution of a *single* 2D model function with a few simple elements accurately represents all collision systems from p-p to central Au-Au. This study presents a description of model properties inferred from 2D histograms by y_t-differential model fits.

C. y_t-differential model function

The y_t-integral $v_2\{2{\rm D}\}(b)$ analysis described in Refs. [14,15] employed an 11-parameter model function as described in Ref. [16]. The 2D histograms were fitted with a data model including several elements applicable to higher RHIC energies and all Au-Au centralities. The 11-parameter model is

$$\begin{aligned}\frac{\Delta\rho}{\sqrt{\rho_{\rm ref}}} = {} & A_{\rm 2D}\exp\left\{-\frac{1}{2}\left[\left(\frac{\phi_\Delta}{\sigma_{\phi_\Delta}}\right)^2 + \left(\frac{\eta_\Delta}{\sigma_{\eta_\Delta}}\right)^2\right]\right\} \\ & + A_D[\cos(\phi_\Delta - \pi) + 1]/2 + A_0 \\ & + A_Q 2\cos(2\phi_\Delta) + A_{\rm soft}\exp\left\{-\frac{1}{2}\left(\frac{\eta_\Delta}{\sigma_0}\right)^2\right\} \\ & + A_{\rm BE}\exp\left\{-\left[\left(\frac{\phi_\Delta}{w_{\phi_\Delta}}\right)^2 + \left(\frac{\eta_\Delta}{w_{\eta_\Delta}}\right)^2\right]^{1/2}\right\}. \quad (11)\end{aligned}$$

The definitions of two parameters in that expression (A_D and A_Q) are slightly modified from those in Ref. [16].

For the present y_t-differential analysis we introduce three changes to the fit model. (a) We switch from per-particle measure $\Delta\rho/\sqrt{\rho_{\rm ref}}$ to per-pair measure $\Delta\rho/\rho_{\rm ref}$ to facilitate comparisons with published $v_2(p_t)$ data from 1D methods while not requiring corrected SP spectra $\rho_0(y_t,b)$. (b) We eliminate one NF element not required to describe more-

central Au-Au collisions. (c) We introduce an alternative Gaussian model for the AS 1D peak.

With y_t cuts imposed jet-related peak structures may become narrower, as expected for jet correlations and observed in so-called trigger-associated dihadron correlations [38,39]. If the AS 1D peak on azimuth narrows its Fourier series representation may require more than a single AS dipole term, and an AS 1D Gaussian may be a more-efficient representation. A narrower AS 1D peak may also introduce a systematic ambiguity between the NJ quadrupole and a jet-related quadrupole contribution from the narrower AS peak [40]. In this analysis each of two AS 1D peak models is included alternately in 2D model fits. Any differences in inferred $B_Q\{2D\}(y_t,b)$ values provide an estimate of systematic uncertainties.

Given that context, we simplify the 2D data model for several reasons: (a) The y_t-differential analysis includes 99 histograms each for 62 and 200 GeV and for two AS peak models. Each of nearly 400 conditions then requires up to 1000 fits with random starting parameters to ensure location of *global* χ^2 minima. The entire analysis program is executed several times to investigate data quality, alternative data models, and overall fit stability. Of order 10^6 fits are then required. (b) With data subdivided into 11 centrality bins and 9 y_t bins, the statistical power for each fit is reduced. (c) In this analysis we emphasize quadrupole systematics for more-central Au-Au collisions where some of the NF terms in Eq. (10) are not required for accurate data description. For those reasons a model with fewer parameters is permitted and provides improved fit stability and more-rapid convergence.

The per-particle model in Ref. [16] includes 11 parameters, of which only 5 or 6 parameters represent physically relevant model elements [SS 2D peak (3), AS 1D peak (1 or 2), NJ quadrupole (1)]. The remainder are mainly required for structure prominent only in peripheral A-A and p-p collisions. The soft-component term $A_{\rm soft}\exp\{-\eta_\Delta^2/2\sigma_s^2\}$ (two parameters), included in the present study for more-peripheral collisions, is not required for more-central Au-Au collisions. In y_t-integral analysis the amplitude of that term is observed to fall to zero above midcentrality (50% fractional cross section) [16]. We drop the model element representing BEC + electron pairs (three parameters) because that structure becomes very narrow in more-central Au-Au collisions. To compensate, three histogram bins near the $(\eta_\Delta,\phi_\Delta)$ origin are removed from the 2D fits to eliminate sensitivity to the narrow BEC + electron-pair component.

The 2D model function for y_t-differential analysis applicable to more-central A-A collisions is then [17]

$$\frac{\Delta\rho}{\rho_{\rm ref}} = B_0 + B_{2D}\exp\left\{-\frac{1}{2}\left[\left(\frac{\phi_\Delta}{\sigma_{\phi_\Delta}}\right)^2+\left(\frac{\eta_\Delta}{\sigma_{\eta_\Delta}}\right)^2\right]\right\} + B_D\{1+\cos(\phi_\Delta-\pi)\}/2 + B_Q 2\cos(2\phi_\Delta), \quad (12)$$

where B_0 is a constant offset and $B_Q \to B_Q\{2D\} = v_2^2\{2D\}$ denotes the NJ quadrupole derived from model fits to 2D angular correlations. The soft-component term with amplitude $B_{\rm soft}$ does not appear explicitly in Eq. (12) but is included in model fits to more-peripheral data histograms. Equation (12) is then referred to as the *eight-parameter model*.

As noted, the AS 1D peak can be modeled by an AS 1D Gaussian or by its limiting case, an AS dipole [as in Eq. (12)] [32,40]. If the AS dipole is chosen the inferred quadrupole amplitude determines an upper limit on the true *NJ* quadrupole. If the AS 1D Gaussian is chosen the inferred quadrupole determines a lower limit. The difference estimates systematic uncertainties for $v_2^2\{2D\}(y_t,b)$. The 2D fit model also includes image Gaussians at 2π for the SS 2D Gaussian and at $-\pi$ for the AS 1D Gaussian if that peak model is employed [40].

Amplitudes are denoted by symbol B_X in the 2D fit model of Eq. (12) applied to per-pair data histograms $\Delta\rho/\rho_{\rm ref}$ as opposed to amplitudes A_X for per-particle histograms. From model fits to 2D angular correlations we measure pair ratio $B_Q\{2D\}(y_t,b) = v_2^2\{2D\}(y_t,b)$ and may convert those data to power-spectrum elements $V_2^2(y_t,b)$ via corrected SP y_t spectra $\rho_0(y_t,b)$ (3D densities) and yields $\rho_0(b)$ (2D densities).

V. 2D ANGULAR AUTOCORRELATIONS

In this section we introduce data histograms as 2D angular autocorrelations. The basic analysis procedure is described in Ref. [16]. Charged hadrons from Au-Au collisions at $\sqrt{s_{NN}} = 62$ and 200 GeV accepted for this analysis fell within a detector acceptance defined by $p_t > 0.15$ GeV/c, $|\eta| < 1.0$, and 2π azimuth. Charge signs were determined but particle identification was not otherwise implemented. Further details of track definitions, efficiencies, and quality cuts are described in Ref. [16]. Data for this analysis were selected from earlier RHIC running periods where low luminosities ensure reduced pileup distortions in 2D angular correlations. Reduction of pileup effects and other tracking details are described in Ref. [16]. In this presentation we emphasize the 200-GeV data; the results for 62 GeV are similar modulo the energy-dependence factor reported in Refs. [14,15].

A. y_t-differential 2D histograms

Figure 4 shows example y_t-differential 2D angular autocorrelations for nominal 40%–50%-central 200-GeV Au-Au collisions. The midcentral case is chosen to illustrate typical model fits over a range of y_t bins. The y_t-differential analysis is based on 6.7M and 14.5M (both year 2004, M = 1×10^6) Au-Au collisions at $\sqrt{s_{NN}} = 62$ and 200 GeV, respectively. The panels represent y_t intervals (a) $y_t < 1.4$, (b) $1.8 < y_t < 2.2$, (c) $2.6 < y_t < 3.0$, and (d) $3.4 < y_t < 3.8$ (y_t bins 1, 3, 5, 7).

The BEC-electron peak dominates correlations in the lowest y_t bin, as expected. That peak is wide enough in the lowest bin that it interferes with the SS 2D jetlike peak and degrades the fit quality. Because the information obtained on jet structure in the lowest y_t bin is minimal, fit values for SS 2D peak parameters from that bin are omitted from the rest of the analysis. For larger-y_t bins the BEC-electron peak is reduced in amplitude and widths. A few histogram bins nearest the origin are removed from the fits and the 2D fit model includes no corresponding element. NJ quadrupole data are insensitive to that issue and are retained for all y_t bins.

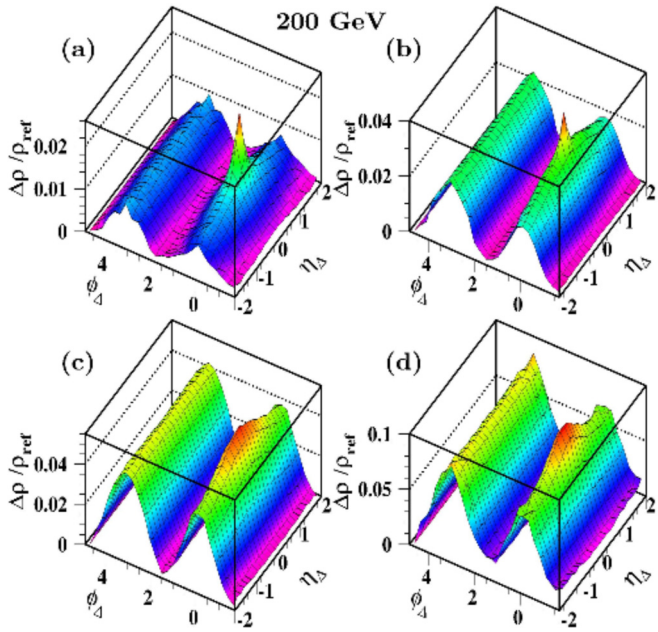

FIG. 4. (Color online) 2D data histograms from 40%–50% central 200-GeV Au-Au collisions for four y_t bins: (a) $y_t < 1.4$, (b) $1.8 < y_t < 2.2$, (c) $2.6 < y_t < 3.0$, (d) $3.4 < y_t < 3.8$. The narrow BEC + electron peak at the origin decreases to zero amplitude for larger y_t.

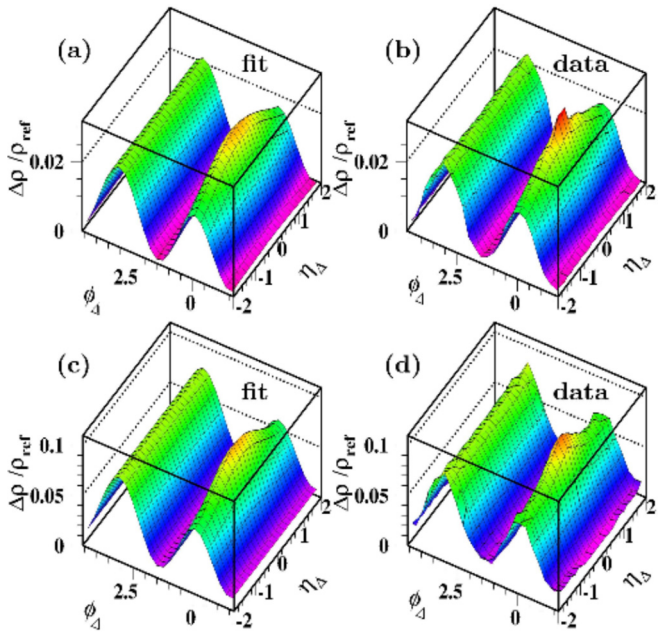

FIG. 5. (Color online) Fits to 2D data histograms from 40%–50% central 200-GeV Au-Au collisions for two y_t bins: (a), (b) $1.8 < y_t < 2.2$ and (c), (d) $3.4 < y_t < 3.8$. The model fits appear on the left in each case. The vertical scale is the same for fits and data. The upper limit has been adjusted to reveal the BEC + electron contribution excluded from the fit (narrow peak in three central bins).

B. Example 2D model fits to y_t-differential data

Figure 5 compares fits (left panels) with data histograms (right panels) for two y_t bins from 40%–50% central 200-GeV Au-Au collisions. That figure presents 2 of 99 cases (11 centralities × 9 y_t bins). For each case approximately 1000 fits starting with randomly chosen initial parameter values are performed. The fit corresponding to the global-minimum χ^2 value is then chosen. The fits were performed with the eight-parameter model function of Eq. (12) including an AS dipole 1D peak model or with a nine-parameter model including an AS Gaussian. The three bins at the origin containing the BEC + electron peak were excluded from all fits. That contribution is mainly confined to the lowest y_t bin.

Small irregularities appearing near the pair-acceptance boundary $|\eta_\Delta| = 2$ have little effect on error-weighted 2D fits because the statistical uncertainties are largest there. The SS 2D peak may deviate from an ideal 2D Gaussian for some applied p_t cuts, but for this analysis of the marginal distribution on y_t the deviations are not substantial. The NJ-quadrupole component is found to be insensitive to such deviations (see Sec. X for further discussion).

VI. y_t-DIFFERENTIAL $B_X\{2D\}$ SYSTEMATICS

Figure 6 shows the y_t and centrality evolution of four fit parameters from 200-GeV Au-Au collisions describing SS 2D peak properties and the NJ-quadrupole amplitude. The plots show per-pair SS 2D peak amplitude B_{2D}, SS peak widths σ_{η_Δ}

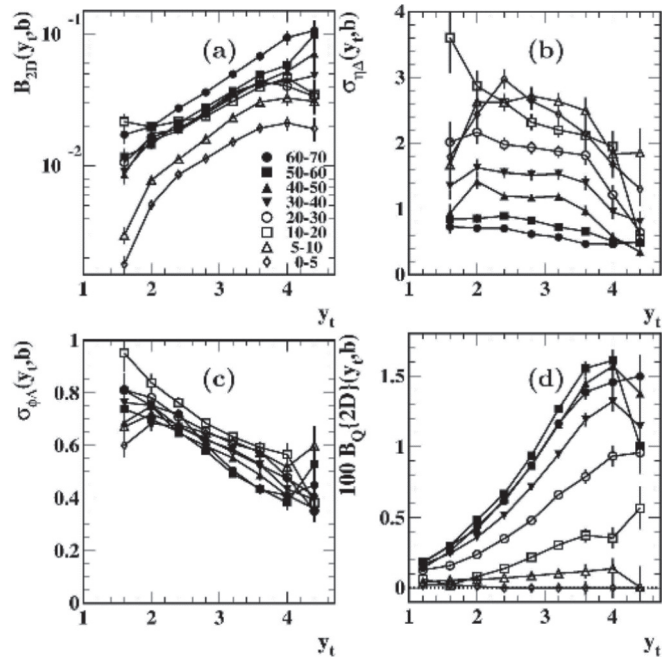

FIG. 6. Per-pair fit parameters derived from 2D fits with Eq. (12) to y_t-differential data histograms from 200-GeV Au-Au collisions for eight centrality bins (0%–70% central). (a) SS 2D peak amplitude $B_{2D}(y_t,b)$; (b),(c) SS 2D peak rms widths $\sigma_{\eta_\Delta}(y_t,b)$ and $\sigma_{\phi_\Delta}(y_t,b)$; (d) per-pair quadrupole amplitude $B_Q\{2D\}(y_t,b)$. The error bars indicate fit uncertainties. The B_Q errors for $y_t = 4.4$ are consistent with a 20% systematic uncertainty for that y_t value, as noted in Sec. X B.

and σ_{ϕ_Δ}, and per-pair NJ-quadrupole amplitude $B_Q\{2D\}$. The data for SS 2D peak properties are not plotted for the first y_t bin ($p_t \approx 0.2$ GeV/c) because correlation structure for that centrality is dominated by the narrow peak representing BEC and conversion electrons [see Fig. 4(a)]. The y_t interval for this analysis includes almost all significant jet correlation structure. The y_t-differential SS 2D peak parameters are required for the $v_2\{2\}(y_t,b) \leftrightarrow v_2\{2D\}(y_t,b)$ comparisons in Sec. XI C. These results are consistent with those of Ref. [17].

The B_{2D} and B_Q data are dominated by trends generally expected for per-pair amplitudes: (a) decrease with increasing centrality and (b) increase with increasing y_t, both owing to the SP $\rho_0(y_t,b)$ spectrum factor in the denominators of the B_X. Smaller physically meaningful variations are overshadowed by the dominant per-pair trends. Just as for $A_Q\{2D\}(b)$ the $B_Q\{2D\}(y_t,b)$ data exhibit remarkable simplicity, but the simplicity is not revealed until we present these results in alternative plotting contexts. Note that $B_Q\{2D\}$ values for 0%–5% central collisions are consistent with zero for almost all y_t bins (at both collision energies), with small upper limits.

In Refs. [14,15] it was reported that y_t-integral per-particle NJ-quadrupole amplitude $A_Q\{2D\}(b,\sqrt{s_{NN}})$ is factorizable, the factors having simple functional forms. With the y_t-differential data from this study we demonstrate that the y_t or p_t dependence of the NJ quadrupole is also factorizable, leading to a simple quadrupole parametrization accurate over a large kinematic space as presented in Sec. IX.

The sharp transition in jet-related angular structure near 50% Au-Au centrality ($\nu \approx 3$) [16] does not significantly alter the p_t structure of the SS 2D peak. Similar y_t trends are observed down to p-p collisions for SS 2D peak and quadrupole despite a substantial change in the SS 2D peak angular shape. To further explore the NJ-quadrupole data systematics, we introduce the concepts of quadrupole source boost and quadrupole spectrum

VII. QUADRUPOLE SOURCE BOOST

The broad source-boost distribution reflecting Hubble expansion of a bulk medium assumed in conventional hydro descriptions is contrasted with a narrow quadrupole source-boost distribution inferred from $v_2(y_t)$ data.

A. Theoretical context

According to hydro descriptions, elliptic flow is an azimuthal modulation of radial flow corresponding to the IS matter eccentricity of noncentral A-A collisions, the transverse flows arising from large pressure gradients in a dense medium [3,41]. Within the hydro narrative most hadrons (especially below 2–3 GeV/c) emerge by "freeze-out" from the monolithic flowing medium, and each hadron is therefore associated with a particular medium speed or relativistic boost corresponding to its freeze-out space-time position. Almost all final-state hadrons should then reflect the same hadron-source boost distribution.

As noted in Ref. [3], if all hadrons emerged from a cylindrical shell with fixed radial speed (as a limiting case), the SP p_t spectrum should exhibit a peak at nonzero p_t and

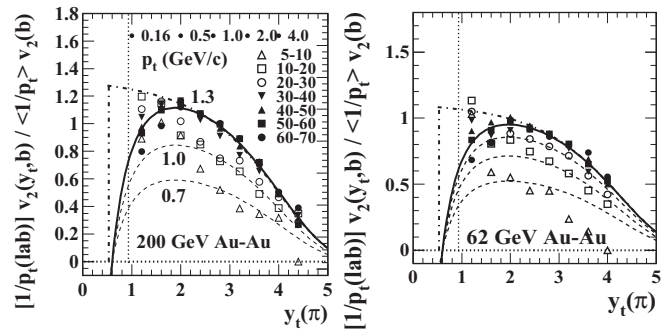

FIG. 7. (Left) Per-pair data $B_2\{2D\}(y_t,b)$ from the present analysis scaled as described in the text and compared with the minimum-bias pion data (solid curve) from Ref. [18] (left panel). The vertical dotted lines mark the TPC acceptance edge on y_t for pions at $p_t = 0.15$ GeV/c. (Right) The same procedure applied to data from 62-GeV Au-Au collisions.

a minimum at zero, reflecting the radial boost of the hadron source. On transverse-rapidity y_t the spectrum alteration would be especially simple: The hadron spectrum in the stationary laboratory frame would be the spectrum in the moving boost frame shifted to larger y_t. For $v_2(p_t)$ the consequence would be negative values for p_t near zero [18]. However, such trends are not expected owing to "more-realistic [hadron source] velocity profile, [wherein] the peak in transverse-momentum distribution disappears." The "more-realistic" velocity profile is approximated by that expected for transverse Hubble expansion of a flowing bulk medium, a broad distribution on radial speed β_t extending from zero to some maximum value. However, so-called "mass ordering" of $v_2(p_t)$ at lower p_t should survive as a manifestation of radial flow.

In Ref. [18] it was pointed out that the ratio $v_2(p_t)/p_t$ for several hadron species plotted vs y_t with the proper mass for each hadron species reveals a common source-boost distribution for identified hadrons from a minimum-bias distribution of Au-Au collisions (centrality-averaged result). The factor $1/p_t$ emerges from a Taylor expansion of the Cooper-Frye expression [42] for the thermal spectrum from a boosted source. Here we consider the centrality dependence of source boosts inferred from $v_2\{2D\}(y_t)$ data for unidentified hadrons from 62- and 200-GeV Au-Au collisions.

B. Quadrupole source-boost centrality dependence

Figure 7 (left panel) shows the source-boost centrality evolution of y_t-differential unidentified-hadron $B_Q\{2D\}$ data from Fig. 6(d) for 200-GeV Au-Au collisions. The plotted quantity is unit-normal ratio $(1/p_t)B_Q\{2D\}(y_t,b)/\langle 1/p_t\rangle B_Q\{2D\}(b)$. The ratio format removes the y_t-integral $v_2(b)$ centrality dependence reported in Refs. [14,15] [see Eq. (7)], bringing data trends near the spectrum mean $\bar{p}_t$ ($\bar{y}_t \approx 1.8$) into alignment at unity. The solid curve represents a centrality-averaged pion curve from Ref. [8] for quadrupole source boost $\Delta y_{t0} = 0.6$ divided by $\langle 1/p_t\rangle \overline{v_2\{2D\}(b)} \approx 0.1$ that describes most of the scaled $B_Q\{2D\}(y_t,b)$ data well.

Figure 7 (right panel) shows the same procedure applied to data from 62-GeV Au-Au collisions. The results are very

similar, with some small quantitative differences noted below. The y_t-integral values $v_2\{2D\}(b)$ used for both plots are derived from Refs. [14,15] for the two energies, and see Sec. XII B. In both cases $\langle 1/p_t \rangle = 2$ (GeV/c)$^{-1}$ and the quadrupole source boost is consistent with $\Delta y_{t0} = 0.6$.

The solid and dashed curves in Fig. 7 are defined by $F(y_t) = g(b)C\{[1 - \beta_t/\tanh(y_t)]/(1 - \beta_t)\}\exp(-p_t/P)$. The expression in curly brackets is determined only by relativistic kinematics and Δy_{t0} [18]. The other factors are derived from data. Factor C is 1.3 and 1.1, respectively, for the two energies. Factor $g(b)$ is defined in Sec. IX. The product $g(b)C$ for three $g(b)$ values (0.55, 0.75, 1.0) is noted next to the curves (left panel). Exponential constant P is 4 ± 0.2 GeV/c for 200 GeV and 5 ± 0.2 GeV/c for 62 GeV. The increase in P for the lower energy may result from the softer SP spectrum in the v_2 denominator: the spectrum hard component at 62 GeV is 60% of the hard component at 200 GeV [16,29], tending to elevate the plotted v_2 ratio at larger y_t.

The plotting format in Fig. 7 includes prefactor $1/p_t$(lab) derived from the measured laboratory p_t. Motivation for that factor relates to interest in the y_t spectrum in the boost frame. In the function $F(y_t)$ the kinematic factor in curly brackets represents the ratio p_t(boost)$/p_t$(lab) relating p_t in the laboratory frame to p_t in the boost frame, as derived in Ref. [18], Eq. (15). If the kinematic factor were removed [i.e., if $1/p_t$(boost) were applied as the prefactor], most of the data would follow the dash-dotted curves.

Within the conventional hydro narrative, one should expect increasing source boosts in more-central A-A collisions as IS particle and energy densities, and therefore density gradients, increase. The data in Fig. 7 suggest that all scaled $B_Q(y_t,b)$ data below 20% central Au-Au centrality are statistically identical in shape. The ratio data follow a simple exponential form that facilitates the universal parametrization described in Sec. IX. Uniformity across most centralities suggests that the quadrupole source boost is approximately independent of Au-Au centrality. Those conclusions are consistent with more-recent Λ $v_2(p_t)$ data [43] for central Au-Au collisions that show the same source boost as the centrality-averaged data [44,45]. We pursue that possibility with differential study of quadrupole spectra.

VIII. QUADRUPOLE SPECTRA

We next consider the centrality dependence of azimuth quadrupole spectrum shapes above $p_t = 0.5$ GeV/c. Ratio measure $v_2\{\text{method}\}(y_t,b)$ includes the SP y_t spectrum $\rho_0(y_t,b)$ in its denominator. The SP spectrum has a strong jet contribution (spectrum hard component) [46] that should not relate to hydro models and is then generally extraneous to the azimuth quadrupole problem. Depending on the v_2 method, the numerator of $v_2(y_t,b)$ may also include significant contributions from jets in the form of a "nonflow" bias. To study the quadrupole spectrum in isolation we remove the jet contributions from numerator and denominator of v_2 by focusing on NJ-quadrupole amplitude $V_2^2\{2D\}(y_t,b) = \rho_0(b)\rho_0(y_t,b)B_Q\{2D\}(y_t,b)$.

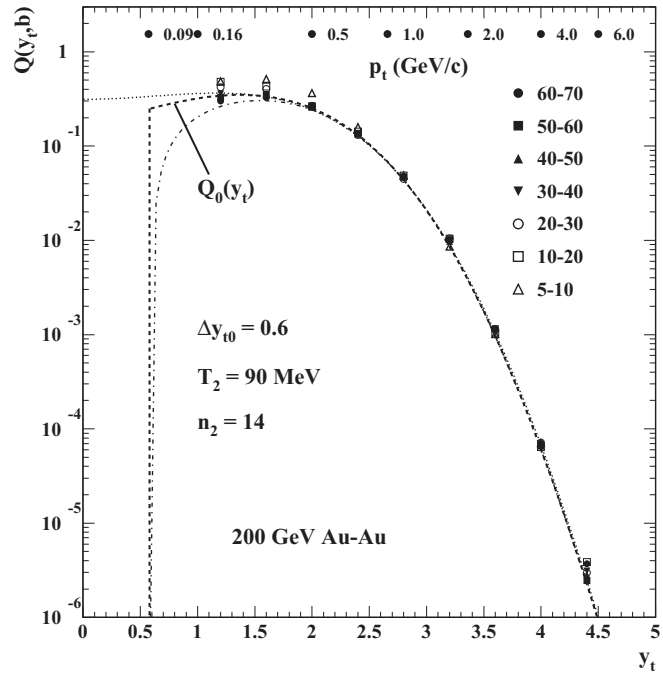

FIG. 8. Unit-normal quadrupole spectra for seven centralities of 200-GeV Au-Au collisions derived from Eq. (13). The spectrum shapes are independent of Au-Au centrality: All $Q(y_t,b)$ coincide within systematic uncertainties. The common shape denoted by $Q_0(y_t)$ is well described by a boosted Lévy distribution with parameters T_2 and n_2 [18].

Based on $B_Q(y_t,b)$ data described in the previous section and Ref. [18], we define a *unit-normal* ratio

$$Q(y_t,b) \equiv \frac{(1/p_t)V_2^2\{2D\}(y_t,b)}{\langle 1/p_t \rangle V_2^2\{2D\}(b)} \to \frac{(1/p_t)\rho_0(y_t,b)v_2\{2D\}(y_t,b)}{\langle 1/p_t \rangle \rho_0(b)v_2\{2D\}(b) \times g(b)}, \quad (13)$$

where the data from the present analysis are of the form $B_Q\{2D\}(y_t,b) = v_2\{2D\}(b)v_2\{2D\}(y_t,b)$. We seek the centrality dependence of the quadrupole *spectrum shape* represented by $Q(y_t,b)$. The *ad hoc* $O(1)$ factor $g(b)$ in the second line is defined and discussed in Sec. IX.

Figure 8 shows $Q(y_t,b)$ data for seven centrality bins of 200-GeV Au-Au collisions derived from pair ratios $B_Q(y_t,b)$ obtained in the present analysis (Fig. 6). Two-dimensional model fits with the AS dipole peak model are preferred because those fits are more stable. The B_Q data are combined with SP spectra $\rho_0(y_t,b)$ and yields $\rho_0(b)$ from Ref. [46] to compute $Q(y_t,b)$. The ratio is undefined for the 0%–5% bin because $v_2\{2D\}(y_t,b)$ for that centrality is consistent with zero for $y_t > 2$. We observe that, within the data uncertainties, y_t-differential quadrupole data follow a universal spectrum shape above $y_t = 2$ ($p_t = 0.5$ GeV/c), represented by unit-normal quadrupole spectrum $Q_0(y_t)$ (dashed curve) previously derived from minimum-bias particle-identified (PID) v_2 data in the form of a *boosted Lévy distribution* [18]. Q_0 is *not a fit* to data from the present analysis. We conclude that quadrupole source boost $\Delta y_{t0} \approx 0.6$ for unidentified hadrons (mainly pions) is

approximately *independent of Au-Au centrality*. That result is consistent with 0%–10% Λ $v_2(p_t)$ data from Ref. [43].

There are currently no accurate parametrizations available for 62-GeV SP spectra $\rho_0(y_t,b)$. Thus, complete reconstruction of quadrupole spectra for the lower energy is not possible. Based on the results in Fig. 7, the same quadrupole spectrum universality may persist there.

In Fig. 7 we observed that the plotted data for the three most-central bins in the interval $y_t > 2$ ($p_t > 0.5$ GeV/c) are suppressed relative to the trend for other centralities. In Fig. 8 those data have been rescaled by factors $g(b)$ in Eq. (13). The resulting vertical shifts bring the spectra into coincidence above $y_t = 2$. The agreement of all quadrupole spectrum shapes with common form $Q_0(y_t)$ over that interval is within data uncertainties. The y_t-integral quantity $v_2\{2D\}(b)$ from Ref. [15] is consistent with the $v_2\{2D\}(y_t,b)$ values below $y_t = 2$ for all centralities (because of the SP spectrum shape), but a substantially different $v_2'(b)$ describes the $v_2(y_t,b)$ centrality trend above $y_t = 2$ for more-central collisions.

Results from Ref. [18] and Fig. 8 taken together suggest that all quadrupole spectra for any A-A centrality and for any hadron species follow universal $Q_0(m_t')$ in the boost frame, except for most-central Au-Au collisions, where an additional reduction factor $g(b) < 1$ is required. That conclusion may be contrasted with arguments for quark-number scaling of $v_2(p_t)$ data summarized in Ref. [18].

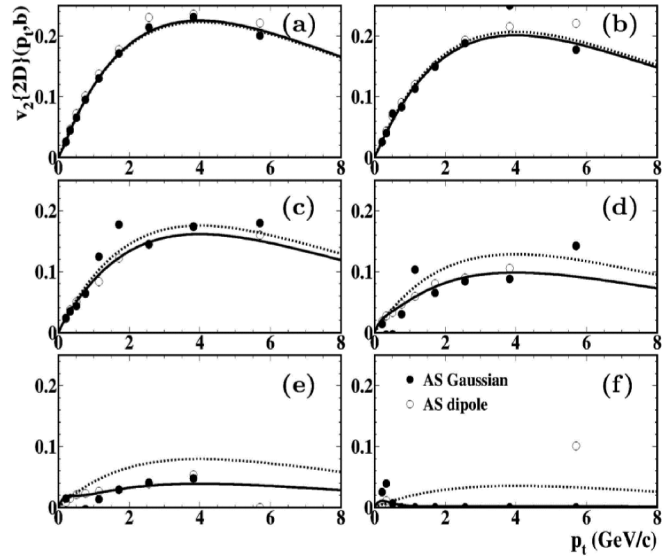

FIG. 9. p_t-differential $v_2\{2D\}(p_t,b)$ trends from 200-GeV Au-Au collisions (points) compared to a parametrization of $v_2\{2D\}(p_t,b)$ data given by Eq. (16) (solid curves) for (a) 40%–50%, (b) 30%–40%, (c) 20%–30%, (d) 10%–20%, (e) 5%–10%, (f) 0%–5% centralities. Solid points are for the AS 1D Gaussian peak model and open circles are for the AS dipole peak model in Eq. (12). Dotted curves are Eq. (16) without factor $f(y_t,b)$.

IX. $v_2(y_t,b,\sqrt{s_{NN}})$ PARAMETRIZATION

Model-parameter trends derived from 2D model fits to y_t-differential histograms reveal factorization of quadrupole systematics on centrality and hadron y_t, the factors described by simple functions.

Combining above results the y_t-differential quadrupole amplitude can be described in factorized form as

$$V_2^2\{2D\}(y_t,b) \approx \langle 1/p_t\rangle(b) V_2^2\{2D\}(b) p_t Q_0(y_t). \quad (14)$$

That simplicity becomes apparent only in terms of extensive measure $V_2^2(y_t,b)$ obtained by eliminating the SP spectrum in the denominator of intensive measure $v_2^2(y_t,b)$ with its strong jet contribution. The simplicity of Eq. (14) is unique to the quadrupole spectrum.

The quadrupole amplitude determined in this study is

$$B_Q\{2D\}(y_t,b) = v_2^2\{2D\}(y_t,b) = v_2\{2D\}(b)\, v_2\{2D\}(y_t,b), \quad (15)$$

and we use the $v_2\{2D\}(b)$ parametrization from Refs. [14,15] (Sec. XII B) to infer $v_2\{2D\}(y_t,b)$. Based on Sec. VIII the $v_2\{2D\}(y_t,b)$ data can be represented accurately by a simple parametrization, just as for the y_t-integral case. From above we have the relation $V_2^2(y_t,b) = \rho_0(b)\rho_0(y_t,b)v_2^2(y_t,b)$. Rearranging Eq. (14) accordingly, we obtain the parametrization

$$v_2\{2D\}(p_t,b) = p_t\langle 1/p_t\rangle v_2\{2D\}(b)\left\{\frac{Q_0(p_t)}{\rho_0(p_t,b)/\rho_0(b)}\right\}$$

$$\frac{Q_0(p_t)}{\rho_0(p_t,b)/\rho_0(b)} \approx \exp(-p_t/P)\times f(y_t,b), \quad (16)$$

which can be compared with $v_2(p_t,b)$ data. The ratio of unit-normal spectra in curly brackets is approximated with reasonable accuracy by $\exp(-p_t/P)$. An $O(1)$ empirical factor $f(y_t,b)$ representing deviations from that function for more-central collisions is

$$f(y_t,b) = 1 + C(b)[\mathrm{erf}(y_t - 1.2) - \mathrm{erf}(1.8 - 1.2)]$$
$$C(b) = 0.12 - (\nu - 3.4)/5 - [(\nu - 3.4)/2]^5. \quad (17)$$

Function $f(y_t,b)$ decreases with y_t from values exceeding 1 for $y_t < 2$ to a constant value $g(b) \leqslant 1$ for $y_t > 2$. The curve crosses through unity near $y_t = 1.8$ ($p_t \approx 0.4$ GeV/c). Values $g(b) = 0.9, 0.75, 0.55$ are inferred from the data for centrality bins 20%–30% through 5%–10% (the 0%–5% B_Q data for $y_t > 2$ are consistent with zero).

Figure 9 shows comparisons between Eq. (16) and 200-GeV data from the present y_t-differential analysis (points). The solid dots and open circles represent $v_2\{2D\}\{p_t,b\}$ data from 2D fits with AS 1D Gaussian and AS dipole peak models, respectively. The parametrization of Eq. (16) (solid curves) describes the {2D} data accurately over a large kinematic range. Significant differences arising from the choice of AS 1D peak model appear only for large y_t values, as expected. Thus, the algebraic relations in Refs. [14,15] and Eq. (16) are confirmed by comparisons with these $v_2\{2D\}(y_t,b)$ data.

The dotted curves exclude the factor $f(y_t,b)$ and therefore have the simple form $\propto p_t \exp(-p_t/P)$, with $P = 4$ GeV/c for 200 GeV. The more-peripheral data (possibly down to N-N collisions) are consistent with that parametrization (follow the dotted curves). Nonjet quadrupole data for three more-central bins and, for $y_t > 2$ ($p_t > 0.5$ GeV/c), fall increasingly below the trend predicted by the parametrization of $v_2\{2D\}(b)$ from

Ref. [15], and quadrupole data for 0%–5% central collisions are consistent with zero throughout that interval.

X. SYSTEMATIC UNCERTAINTIES

Statistical and systematic uncertainties are discussed for y_t-differential B_Q data and for inferred quadrupole spectrum trends. For this differential study the choice of fit model is a compromise between minimizing systematic errors and employing the same model to cover large kinematic intervals on y_t and centrality ν. For this discussion, we refer to the model elements in Eq. (12).

A. 2D fit-model elements

At lower y_t the 2D exponential (BEC + electrons) peak narrows with increasing centrality while the SS 2D peak broadens on η, ensuring accurate distinctions. At higher y_t the exponential peak amplitude drops rapidly to zero. Thus, except for peripheral collisions that element can be dropped from the 2D fit model. To minimize systematic fit errors from that source the central three bins are omitted from all 2D fits (bin errors greatly increased).

At small ν (peripheral collisions, below the sharp transition) the SS 2D peak is narrow on η and ϕ and accurately described by a 2D Gaussian for all y_t bins. In more-central Au-Au collisions the SS 2D peak broadens on η but remains narrow on ϕ. For most y_t bins the 2D peak is still accurately described by a 2D Gaussian. At larger y_t the peak is distorted on η_Δ, developing non-Gaussian tails as observed in trigger-associated analysis [38,39]. The 2D Gaussian model, while no longer binwise accurate, does estimate the peak amplitude and rms widths satisfactorily for the present study focusing on the azimuth quadrupole component.

In more-peripheral collisions (and in the y_t-integral analysis) the AS 1D peak is broad enough to be modeled accurately by a single dipole term. In more-peripheral collisions and at larger y_t the AS 1D peak appears to narrow. If the width of the AS peak becomes substantially smaller than $\pi/2$ and the AS dipole model is employed, the quadrupole component of the AS 1D peak might appear as a bias in the inferred quadrupole amplitude. That bias source can be investigated by replacing the AS dipole with an AS 1D Gaussian model and refitting the 2D data. Any differences in inferred $B_Q\{2D\}(y_t,b)$ establish the systematic uncertainty from that source in the inferred NJ azimuth quadrupole amplitude, typically at the few-percent level as with other fit uncertainties.

B. 2D fit-quality systematics

Figure 10 shows typical fit residuals for lower- and higher-y_t bins using the eight-parameter fit model. For lower-y_t bins (left panel) the residuals do not contain significant large-scale structure and are generally consistent with statistical uncertainties. The $\chi^2/\mathrm{DoF} \approx 0.8$–$2.5$ (DoF = fit number of degrees of freedom). The BEC + electron peak at the origin appearing in the residuals (not described by the fit model) does not contribute to the χ^2 because those three bins are excluded from the fit (assigned artificially large errors). In the higher-y_t bin the BEC + electron peak is negligible, consistent with the p_t dependence of both mechanisms.

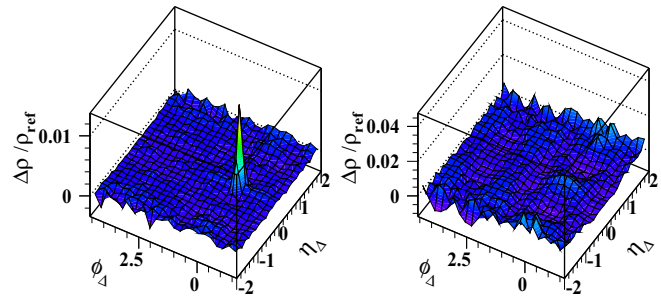

FIG. 10. (Color online) Residuals from 2D fits to y_t-differential histograms from 40%–50% central 200-GeV Au-Au collisions for (left) $y_t \in [1.8,2.2]$ ($p_t \in [0.4,0.65]$ GeV/c) and (right) $y_t \in [3.4,3.8]$ ($p_t \in [2,3.3]$ GeV/c). The vertical scales are half the range of the corresponding panels in Fig. 4.

To summarize systematic uncertainty trends for the y_t-differential analysis, we identify three zones on kinematic space (y_t,ν). Zone A is more-peripheral collisions ($\nu < 2$, $1 - \sigma/\sigma_0 \leqslant 0.3$) for all y_t, zone B is more-central collisions ($\nu > 2$) for lower y_t, and zone C is more-central collisions for higher y_t. The y_t boundary between zones B and C is approximately $y_t = 3.8$ ($p_t \approx 3$ GeV/c). In zone A the 11-parameter model function for y_t-integral analysis from Refs. [15,16] is required for satisfactory fits. In zone B either the 11- or 8-parameter model function provides similar fit quality.

In zone C the 11-parameter model is excluded because of fitting ambiguities between part of the SS 2D peak structure and the 2D exponential model element, but the simpler 8-parameter model function provides an adequate description when three bins near the origin are excluded from the fit. As noted, the simpler model function is therefore utilized to cover zones B and C reported in this y_t-differential analysis, and zone A is not reported. Systematic uncertainties in zone B are small and consistent with statistical and fit errors. Uncertainties in C may be significant and are explicitly estimated.

Figure 10 (right panel) shows small but significant residuals structure resulting from the non-Gaussian shape of the SS 2D peak appearing in larger-y_t bins (zone C): excesses at the origin and near the acceptance boundaries on η_Δ for $\phi_\Delta \approx 0$. A small excess in the *inferred* quadrupole B_Q is also observed (e.g., depression near $\phi_\Delta = \pi$) owing to the non-Gaussian SS peak shape. The peak-peak residual quadrupole amplitude is about 0.001 for $B_Q \approx 0.014$ [Fig. 6(d)]. Thus, the relative uncertainty is $\approx 0.0005/0.014 \leqslant 5\%$, comparable to the typical fit uncertainties there. The inferred quadrupole data are generally stable against minor changes in jet-related fit-model elements or the SS 2D peak shape, except for the largest y_t value (4.4), where a substantial systematic uncertainty (20%) must be assigned to that single B_Q point for each centrality. What is most important to ensure accuracy of the NJ quadrupole is the presence in the fit model of a SS 2D peak element narrow on the azimuth.

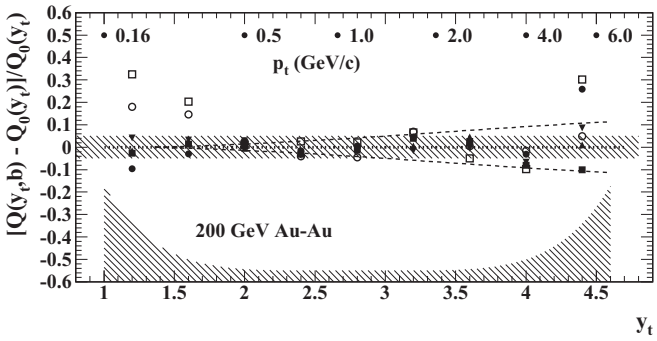

FIG. 11. Data-model deviations $Q(y_t,b) - Q_0(y_t)$ are shown relative to fixed spectrum model $Q_0(y_t)$. The upper hatched band indicates that the rms data deviation is less than 5% except near the acceptance end points. There are systematic deviations below 0.5 GeV/c and larger fitting uncertainties for the largest y_t bin. The lower hatched band provides an estimate of systematic uncertainties above $y_t = 1.8$ and the range of variations corresponding to $v_2(b)$ vs $v_2'(b)$ below $y_t = 1.8$. The dashed curves are explained in the text.

C. Quadrupole spectrum uncertainties

The SP spectrum parametrization from Ref. [46] is not constrained by data below $y_t = 2$. Thus, some systematic deviations from the $Q_0(y_t)$ reference may be attributable to inaccuracies in the modeled SP spectrum structure. Also, we have approximated the hadron spectrum for this study by the pion spectrum alone. Protons and kaons do play a significant role in the hadron spectrum shape, and those spectra are substantially different from the pion spectrum, introducing a further source of systematic bias.

Figure 11 shows relative deviations of unit-normal quadrupole spectrum data $Q(y_t,b)$ from universal spectrum reference $Q_0(y_t)$. The symbols are defined as in Fig. 8. The more-central data are scaled by factor $g(b) < 1$ as in Fig. 8 so that spectrum shapes for $y_t > 2$ ($p_t > 0.5$ GeV/c) can be compared. The more-central data then exhibit large deviations below $y_t = 2$ owing to the rescaling. Such deviations could represent variations in SP spectra below $y_t = 2$, but they may also reflect significant changes in the actual quadrupole spectra with physical implications. The deviations above $y_t = 4$ are consistent with fit instabilities and sparse statistics. However, we also expect an excess at larger y_t because those data are derived using the AS dipole model. If the AS 1D peak narrows at larger y_t (expected) the quadrupole component of the AS 1D peak may then contribute a positive bias to the inferred $v_2\{2D\}$ data.

We can establish an upper limit on possible source-boost variations with a Taylor expansion of $Q(y_t,b)$ about $Q_0(y_t)$ relative to variations in boost Δy_{t0}. The two dashed curves represent $\pm\delta y_{t0}\, d\log[Q_0(y_t)]/dy_t$, with $\delta y_{t0} = 0.02\Delta y_{t_0} = 0.012$ or 2% of the mean source boost. The data lie well within those limits for $y_t > 1.8$ ($p_t > 0.4$ GeV/c). Boost variations with centrality are comparable to or smaller than those observed small deviations on y_t. The comparison suggests that the mean quadrupole source boost does not change by more than a few percent over a broad centrality interval. In general, the $Q_0(y_t)$ universal quadrupole spectrum represents the $Q(y_t,b)$ data well over p_t in 0.35–4 GeV/c (y_t in 1.8–4).

XI. COMPARISONS AMONG v_2 METHODS

Substantial differences appear between the NJ azimuth quadrupole $v_2\{2D\}$ derived from model fits to 2D angular correlations and $v_2\{\text{method}\}$ data derived from conventional NGNM (equivalent to 1D model fits to azimuth correlations) [15,17]. In this section we provide detailed comparisons among several methods and consider possible sources of observed differences.

A. Algebraic relation between $v_2\{2\}$ and $v_2\{\text{EP}\}$

To establish the relation between conventional event-plane {EP} and two-particle correlation {2} methods, we first note that $v_2\{\text{EP}\}$ is defined by [8,26]

$$v_2\{\text{EP}\} = \frac{v_{2,\text{obs}}}{\langle\cos[2(\Psi_2 - \Psi_r)]\rangle}, \tag{18}$$

where the numerator is "observed" $v_{2,\text{obs}}$ (defined below) and the denominator is described as the *event-plane resolution*. To relate $v_{2,\text{obs}}$ to $v_2\{2\}$, we define the $m = 2$ (azimuth quadrupole) Q vector by [26,44,47]

$$\vec{Q}_2 = \frac{1}{2\pi\,\Delta\eta}\sum_{i=1,\in\Delta\eta}^{n}\vec{u}(2\phi_i) \equiv Q_2\vec{u}(2\Psi_2), \tag{19}$$

with unit vectors $\vec{u}(\phi)$ and *event-plane* angle Ψ_2. The vector notation is an alternative to that in Ref. [47] based on complex quantities. $\vec{Q}_2$ as defined in Eq. (19) is a 2D angular density. We then have

$$Q_2^2 = \vec{Q}_2\cdot\vec{Q}_2 = \frac{\rho_0}{2\pi\,\Delta\eta} + V_2^2\{2\}, \tag{20}$$

as in Eq. (4), but *with self-pairs included* in the first term on the right-hand side. It is notable that $V_2^2\{2\}$ and Q_2^2 differ only by the self-pair term. We then have

$$\begin{aligned} v_{2,\text{obs}} &\equiv \langle\cos[2(\phi - \Psi_2)]\rangle \\ &= \frac{1}{n}\sum_{i=1}^{n}\vec{u}(2\phi_i)\cdot\vec{u}(2\Psi_{2,i}),\ \text{or} \\ Q_2' v_{2,\text{obs}} &= \frac{1}{2\pi\,\Delta\eta}\frac{1}{n}\sum_{j\neq i=1}^{n,n-1}\vec{u}(2\phi_i)\cdot\vec{u}(2\phi_j) \\ &= v_2\{2\}V_2\{2\}, \end{aligned} \tag{21}$$

where $Q_2' = Q_2\sqrt{(n-1)/n}$, and $X_{2,i}$ indicates that the ith term is excluded from a sum over j. The summation condition $j \neq i$ in Eq. (21) (third line) excludes self-pairs from that pair sum but *not* from Q_2 in Eq. (20) (or Q_2'). From Ref. [26] we obtain the "event-plane resolution" measure

$$\begin{aligned} \overline{\cos^2[2(\Psi_2 - \Psi_r)]} &= \frac{\overline{n\,V_2^2\{2\}}}{(n-1)\,\overline{Q_2^2}} \\ &\approx \frac{n v_2^2\{2\}}{1 + n v_2^2\{2\}}, \end{aligned} \tag{22}$$

where $n v_2^2\{2\}$ serves as a statistical figure of merit for ratio v_2 analogous to σp^2 (σ is a nuclear cross section) or Lp^2 (L is a beam luminosity) for measurements of polarization ratio p. The $\{\text{EP}\} \leftrightarrow \{2\}$ relation is then

$$v_2\{2\} = v_{2,\text{obs}} \frac{Q_2}{V_2\{2\}} \sqrt{\frac{n-1}{n}} = \frac{v_{2,\text{obs}}}{\langle \cos[2(\Psi_2 - \Psi_r)] \rangle_{\text{rms}}} \approx v_2\{\text{EP}\}. \quad (23)$$

Small $\{\text{EP}\} \leftrightarrow \{2\}$ differences may arise from covariances corresponding to non-Poisson multiplicity fluctuations. The "event-plane resolution" correction is required because invocation of an event-plane estimate via $\vec{Q}_2$ implicitly includes a self-pair contribution. Excluding self-pairs in Eq. (21) does not remove the Q_2 bias. The $v_2\{\text{EP}\}$ estimate does not necessarily relate to an A-A reaction plane; it represents all 2D correlation structure *including jets*. We hereafter refer exclusively to $v_2^2\{2\}$ or $V_2^2\{2\}$ except when introducing published $v_2\{\text{EP}\}$ data.

B. Algebraic relation between $v_2\{2\}$ and $v_2\{2\text{D}\}$

The quadrupole power-spectrum element $V_2^2\{2\}$ (equivalent to $\rho_0 A_Q\{2\}, \rho_0^2 B_Q\{2\}$) represents the total azimuth quadrupole component for all angular correlations, including both jet-related structures and any NJ structure that might be identified with flows. As noted in Sec. IV A, the η_Δ dependence of 2D angular correlations can be employed to separate unique correlation components via 2D model fits, as in Refs. [10,16] and the present analysis. For almost all collision conditions we observe that the AS structure of 2D angular correlations is uniform on η_Δ within $|\eta| < 1$ and completely described by a NJ azimuth quadrupole represented by $A_Q\{2\text{D}\}$ and an AS dipole component.

The only remaining nontrivial structure observed in more-central Au-Au collisions is a SS 2D peak (consistent with intrajet correlations). Because the AS dipole is orthogonal to all other multipoles, the SS 2D peak is the only other significant contributor to total quadrupole $V_2^2\{2\} = \rho_0^2 v_2^2\{2\}$ *in more-central A-A collisions*. The SS 2D peak per-particle quadrupole amplitude (Fourier coefficient) is given by [32]

$$2A_Q\{\text{SS}\}(b) = F_2(\sigma_{\phi_\Delta}) G(\sigma_{\eta_\Delta}; \Delta\eta) A_{2\text{D}}, \quad (24)$$

where $A_{2\text{D}} = \rho_0 B_{2\text{D}}$ is the per-particle amplitude of the fitted SS 2D peak with rms widths $(\sigma_{\eta_\Delta}, \sigma_{\phi_\Delta})$, F_2 is the $m = 2$ Fourier component of a unit-amplitude 1D Gaussian on azimuth with width σ_{ϕ_Δ},

$$2F_m(\sigma_{\phi_\Delta}) = \sqrt{2/\pi}\sigma_{\phi_\Delta} \exp\left(-m^2\sigma_{\phi_\Delta}^2/2\right), \quad (25)$$

and $G \leqslant 1$ is a calculated 2D $\rightarrow$ 1D η projection factor defined in Ref. [32]. We thus obtain the relation

$$A_Q\{2\} = A_Q\{2\text{D}\} + A_Q\{\text{SS}\} \quad (26)$$

plus a small contribution from BEC + electron pairs in more-peripheral collisions. Jet-related quadrupole $A_Q\{\text{SS}\}$ may be identified with "nonflow" [32,33,40]. NJ quadrupole $A_Q\{2\text{D}\}$ would correspond to elliptic flow if that phenomenon is relevant. We test that relation with results from the present and previous 2D correlation analysis and published $v_2\{\text{method}\}$ data in the next section.

Strategies have been adopted to reduce nonflow (mainly jet contributions) to v_2 by excluding some parts of the nominal (η_1, η_2) acceptance from NGNM calculations [32]. For instance, some η_Δ interval centered at zero may be excluded from projections onto ϕ_Δ by "estimating the reaction plane" with large-η detectors [9,48,49]. The motivation is exclusion of jet-related structure $A_Q\{\text{SS}\}$ from azimuth projections $A_Q\{2\}$ *based on assumptions* about the jet fragment distribution on η.

Such η pair cuts may be less effective at distinguishing jet-related structure from a NJ quadrupole than 2D model fits applied within a more-limited η acceptance. In more-central Au-Au collisions the SS 2D peak is strongly elongated and may develop non-Gaussian tails extending over a large η_Δ interval [38]. The effects of η-exclusion cuts are then quite uncertain and may have little impact on jet-related biases in $v_2\{\text{method}\}$ data [32].

C. y_t-differential data comparisons

Figure 12 shows published $v_2^2\{\text{EP}\}(p_t, b)$ data (open circles) compared to $v_2^2\{2\text{D}\}(p_t, b)$ data from the present analysis (solid points or hatched upper limit) and "nonflow" prediction $v_2^2\{\text{SS}\}$ (dash-dotted curve) derived from characteristics of the SS 2D peak measured in this analysis. The $v_2^2\{\text{EP}\}(p_t, b)$ points are obtained by combining $v_2(b)$ and $v_2(p_t, b)$ measurements from Ref. [9]. The hatched region in the left panel denotes an upper limit on $v_2^2\{2\text{D}\}$ [compare with Fig. 9(f)]. The bold solid curve in the right panel is defined (without the factor 100) by $v_2^2\{2\} = v_2^2\{2\text{D}\} + v_2^2\{\text{SS}\}$ per Eq. (26).

We find that the measured $v_2^2\{\text{EP}\} \approx v_2^2\{2\}$ trend is predicted by a combination of $v_2^2\{2\text{D}\}$ data and $v_2^2\{\text{SS}\}$ representing the $m = 2$ Fourier component of the SS 2D jet peak projected onto 1D azimuth. The dash-dotted curves $v_2^2\{\text{SS}\}(p_t, b)$ derived from SS 2D peak properties inferred from this analysis can be interpreted as the jet contribution to $v_2^2\{2\}$. We confirm the

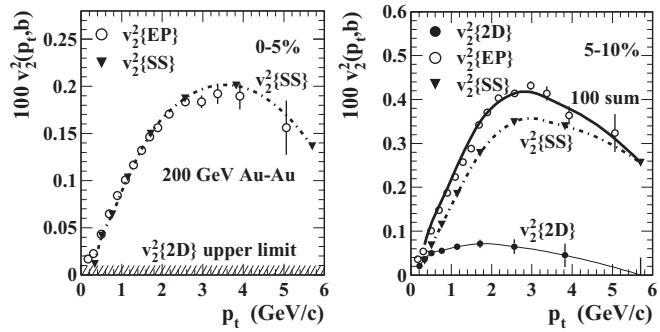

FIG. 12. (Left) Comparison of measured 2D angular correlations represented by $v_2^2\{\text{SS}\}(p_t, b)$ (dash-dotted curve) and $v_2^2\{2\text{D}\}(p_t, b)$ (hatched region, upper limit) with published $v_2^2\{\text{EP}\}(p_t, b)$ data (open circles) for 0%–5% central 200-GeV Au-Au collisions. (Right) Similar comparison for 5%–10% central Au-Au collisions showing the close correspondence between the sum $v_2^2\{2\text{D}\}(p_t, b) + v_2^2\{\text{SS}\}(p_t, b)$ (bold solid curve) and published $v_2^2\{\text{EP}\}(p_t, b)$ data (open circles) as in Eq. (26). The light solid curve through the $v_2^2\{2\text{D}\}$ data (solid dots) represents the parametrization in Eq. (16).

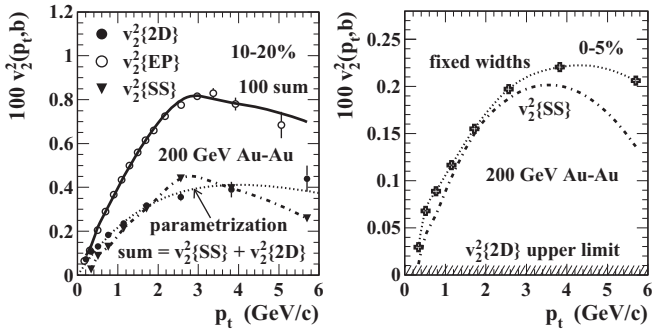

FIG. 13. (Left) Comparison similar to Fig. 12 for 10%–20% central Au-Au collisions showing near-equal contributions from NJ quadrupole $v_2^2\{2D\}(p_t,b)$ and jet-related quadrupole $v_2^2\{SS\}(p_t,b)$. The bold solid curve is the sum of $\{2D\}$ and $\{SS\}$ data. The bold dotted curve is the parametrization of $v_2\{2D\}(p_t,b)$ from Eq. (16) combined with a $v_2\{2D\}(b)$ value derived from Refs. [14,15] (Sec. XII B). (Right) The quadrupole amplitude of the SS 2D peak (dash-dotted curve) derived from Eq. (24) with data from Fig. 6 [same as Fig. 12 (left panel)] compared to a similar calculation using fixed SS 2D peak widths (dotted curve and points). The substantial differences illustrate the importance of accurately measured SS 2D peak properties for understanding jet biases in $v_2\{2\} \approx v_2\{EP\}$ data.

trend $v_2^2\{2\} = v_2^2\{SS\} + v_2^2\{2D\}$ for y_t-differential data based on the detailed η dependence of 2D angular correlations. There is no adjustment to accommodate the $v_2^2\{EP\}$ data.

Figure 13 (left panel) shows data for 10%–20% central Au-Au collisions including similar contributions from NJ quadrupole $v_2^2\{2D\}(p_t,b)$ and jet-related quadrupole $v_2^2\{SS\}(p_t,b)$. The sum (bold solid curve) accurately describes the published $v_2\{EP\}$ data. The parametrization of Eq. (16) (dotted curve) describes the $v_2^2\{2D\}(p_t,b)$ data over the entire p_t acceptance.

Figure 13 (right panel) illustrates the importance of accurate jet-related 2D correlation measurements. The dash-dotted curve is $v_2^2\{SS\}$ from Fig. 12 (left panel) derived from Eqs. (24) and (25) based on measured SS 2D peak characteristics as in Fig. 6. The dotted curve and points represent the same computation with the SS 2D peak widths *held fixed* at $\sigma_{\eta_\Delta} = 2.5$ and $\sigma_{\phi_\Delta} = 0.65$ (y_t-integral values for that centrality). This exercise illustrates that accurate description of the $v_2^2\{EP\}$ data in Fig. 12 (left panel) by the dash-dotted curve relies on full employment of measured SS 2D peak properties.

We learn, for instance, that, relative to the correct dash-dotted curve, the dotted curve assuming fixed SS peak widths is too large at lower p_t because the SS peak azimuth width is substantially larger there, leading to an overestimate of Fourier coefficient $F_2(\sigma_{\phi_\Delta})$ in Eq. (25) by the fixed-width assumption. The dotted curve is too large at higher p_t because the SS peak η-width reduction is not taken into account. The substantial downturn in $v_2^2\{EP\}(p_t,b)$ for 0%–5% centrality at larger p_t is solely attributable to strong narrowing of the SS 2D peak on η_Δ above 4 GeV/c *toward the p-p value*, as in Fig. 6(b). The combination of measured amplitude and widths of the SS peak from Fig. 6 accurately describes the nonflow (jet) contribution $v_2^2\{SS\}$ to $v_2^2\{EP\} \approx v_2^2\{2\}$ (dash-dotted curve).

XII. DISCUSSION

We consider the implications of differential $v_2\{2D\}(y_t,b)$ measurements from this analysis for conventional v_2 measurements and for interpretations of v_2 data in terms of hydrodynamic flows.

A. Fit models and interpretation of model elements

We model y_t-differential 2D angular correlations with Eq. (12) whose elements are motivated only by structures directly observed in the data, with no *a priori* physical assumptions. We then interpret the elements physically by comparison of data systematics with theoretical predictions. Based on measured trends for p-p and more-peripheral A-A collisions (95%–50% fractional cross section), we interpret the SS 2D peak and AS 1D peak elements as "jet-related" (see Sec. II B). All other elements are then referred to as "nonjet," including the NJ azimuth quadrupole. The same terminology is retained in more-central A-A collisions although a jet interpretation may be questioned there. The ordered sequence—mathematical modeling *followed by* physical interpretation—is an essential feature. The jet-related and NJ terminology is complementary to flow-related and nonflow terminology. However, jet phenomenology is well established from extensive HEP measurements and QCD theory, whereas hydrodynamic flows in high-energy nuclear collisions (RHIC and LHC energies as opposed to the Bevalac/AGS energy regime) remain a matter of conjecture (see Sec. XII D for further discussion).

Jet-related and NJ-quadrupole correlation components are separately identified. So-called nonflow bias is associated with the quadrupole ($m = 2$) Fourier component of the jet-related SS 2D peak. $A_Q\{2D\}$ or $B_Q\{2D\}$ results are insensitive to the SS peak shape on η, as noted in the present study. The essential model element is the SS peak 1D Gaussian factor on azimuth, as noted in Ref. [37], where 1D Fourier fits without an SS peak element are strongly rejected by a Bayesian-inference analysis.

B. y_t-integral $A_Q\{2D\}$ systematics

The $A_Q\{2D\}(b,\sqrt{s_{NN}})$ data from Refs. [14,15] reveal two interesting features: (a) Data from two energies are accurately described by the same centrality variation (defined below); (b) the energy dependence of the quadrupole amplitude (in combination with SPS data at 17 GeV [50]) scales as $\log(\sqrt{s_{NN}})$. When plotted on b/b_0 the $A_Q\{2D\}$ data reveal a simple variation closely approximating a Gaussian function centered on $b/b_0 = 0.5$.

Figure 14 (left panel) summarizes the measured NJ-quadrupole energy dependence from Bevalac to highest RHIC energy. A_Q data values at $b/b_0 \approx 0.5$ minimize the relative effects of jet (nonflow) contributions to $A_Q\{\text{method}\}$. We observe a major transition in the energy trend of per-particle measure A_Q near 13 GeV, suggesting *different physical mechanisms* for the measured NJ quadrupole within the two energy regimes [33]. Above 13 GeV the function $R(\sqrt{s_{NN}}) \equiv \log\{\sqrt{s_{NN}}/13.5\ \text{GeV}\}/\log(200/13.5)$ (solid line) describes the energy dependence, with zero intercept at 13.5 ± 0.5 GeV.

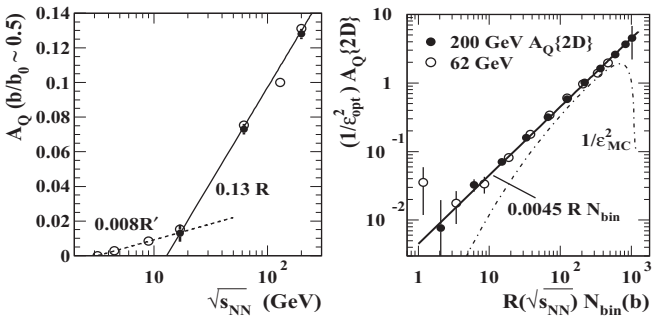

FIG. 14. (Left) Collision energy dependence of v_2 data converted to per-particle measure A_Q. The solid points are from Refs. [14,15] and Ref. [50]. They follow a logarithmic trend proportional to $R(\sqrt{s_{NN}})$ (see text). The Bevalac-AGS trend below 13 GeV is proportional to $R'(\sqrt{s_{NN}}) = \ln(\sqrt{s_{NN}}/3.2\ \text{GeV})$. The open points are taken from Fig. 4 of Ref. [48]. (Right) The azimuth quadrupole amplitude $A_Q\{2D\}$ divided by *optical* ϵ^2_{opt} plotted vs energy-dependent factor $R(\sqrt{s_{NN}})$ times 200-GeV Au-Au binary-collision number $N_{bin}(b)$. The $A_Q\{2D\}$ data are consistent with simple proportionality [Eq. (27)] over three decades.

A similar energy dependence was observed for $\langle p_t \rangle$ fluctuations/correlations attributed to (mini)jets [12] consistent with jet-related trends observed recently at the LHC [51]. The rate of increase with energy (line slopes) is *six times greater* at higher energies than the Bevalac/AGS trend (dashed curve).

Figure 14 (right panel) shows $(1/\epsilon^2_{2,opt})A_Q\{2D\}(b)$ vs $R(\sqrt{s_{NN}})N_{bin}$, where N_{bin} is the number of N-N binary collisions. The vertical-axis variable is motivated to test expectations for the ratio v_2/ϵ: The trend $v_2/\epsilon \propto S dn_{ch}/d\eta$, with S the A-A overlap area for more-peripheral A-A collisions should transition to a "hydro limit" $v_2/\epsilon \approx$ constant in more-central collisions [52]. From the present analysis we conclude that for Au-Au collisions $A_Q\{2D\}$ data above 13 GeV are described by

$$A_Q\{2D\}(b,\sqrt{s_{NN}}) \equiv \rho_0(b) v_2^2\{2D\}(b,\sqrt{s_{NN}}) = C R(\sqrt{s_{NN}}) N_{bin}(b) \epsilon^2_{2,opt}(b), \quad (27)$$

where coefficient C is defined by $1000C = 4.5 \pm 0.2$. Equation (27) accurately describes measured y_t-integral azimuth quadrupole data in heavy-ion collisions for all centralities down to N-N collisions and all energies above $\sqrt{s_{NN}} \approx 13$ GeV. It represents factorization of energy and centrality dependence for the NJ quadrupole. The 2D quadrupole data are also consistent with $V_2^2\{2D\} = \rho_0 A_Q\{2D\} \propto N_{part} N_{bin} \epsilon^2_{2,opt}(b)$ [14], a trend that, modulo the IS eccentricity factor, increases much faster than the dijet production rate. The nonzero value $v_2 \approx 0.02$ from Eq. (27) extrapolated to p-p (N-N) collisions agrees with a p-p color-dipole prediction from QCD theory [53].

C. y_t-differential $A_Q\{2D\}$ systematics

The $B_Q\{2D\}(y_t,b,\sqrt{s_{NN}})$ data from the present study reveal two interesting features: (a) The quadrupole source-boost distribution is independent of Au-Au centrality over a large interval (70% to 5%); and (b) the quadrupole spectrum shape is independent of centrality over the same interval and very different from the SP spectrum shape representing most hadrons. The quadrupole spectrum is much colder (90 MeV vs 145 MeV) and does not change shape above the sharp transition in jet properties as does the SP spectrum (e.g., R_{AA} and "jet quenching"). Those interesting trends are not apparent from the systematics of ratio measure $v_2(p_t)$. Some implications are considered in the next section.

D. Physical implications of $A_Q\{2D\}$ factorization

The present study combined with previous y_t-integral analysis [14,15] reveals two factorizations of the NJ quadrupole denoted by $v_2\{2D\}$: (a) $(b,\sqrt{s_{NN}})$ factorization (y_t-integral case) above 13 GeV; and (b) (y_t,b) factorization at two energies (y_t-differential case). Such factorizations become apparent only in terms of extensive correlation measure V_2^2 and with accurate distinction between the NJ quadrupole and other structure, including jet-related SS 2D and AS 1D peaks.

In case (a) (y_t-integral case) we can aid interpretation by rearranging Eq. (27) to obtain

$$2A_Q = C R(\sqrt{s_{NN}}) \nu(b) \left[N_{part}(b) \epsilon^2_{2,opt}(b) \right]. \quad (28)$$

The left-hand side per-hadron measure of final-state azimuth quadrupole $A_Q\{2D\} = \rho_0 v_2^2$ (momentum space) is mathematically analogous to the right-hand side per-participant IS quadrupole measure within the square brackets (configuration space). The two azimuth correlation measures are simply related by the product of participant path length $\nu(b)$ and energy-dependent factor $R(\sqrt{s_{NN}})$. The quadrupole component of the initial A-A overlap source depends only on impact parameter b. Thus, the final-state NJ quadrupole of produced hadrons (left-hand side) is simply proportional to the IS quadrupole of the collision participants (right-hand side, as determined by $\sqrt{s_{NN}},b,A$) over a large kinematic domain, including N-N (p-p) collisions.

A plot of A_Q vs $1 - b/b_0$ in Ref. [14] suggests that the centrality dependence in Eq. (27) may depend only on the *relative* impact parameter b/b_0 independent of collision energy. The shape of the quadrupole centrality trend may not depend on the absolute size of the collision system, only on the relative geometry of intersecting spheres independent of atomic number A. Further studies with lighter nuclei (e.g., Cu-Cu) may test that hypothesis.

In case (b) (y_t-differential case) we observe that a fixed quadrupole spectrum shape is a universal feature of Au-Au collisions over most of the centrality range (70%–5%), and the inferred source-boost distribution is narrow with fixed mean value. Both results contrast strongly with hydro expectations. In the conventional hydro narrative [3] (i) almost all hadrons emerge from a monolithic flowing bulk medium and (ii) flows are driven by pressure gradients corresponding to large IS energy densities in more-central A-A collisions. Item (i) implies that quadrupole spectra should be equivalent to SP spectra (and thus cancel in ratio v_2), that both phenomena should reflect a broad source-boost distribution corresponding to Hubble expansion of the bulk medium, and that there should be a close relation with the systematics of "jet quenching" in

the medium. Item (ii) implies that flow magnitudes should increase strongly with A-A centrality, may be negligible in more-peripheral collisions, and should correspond with jet-quenching systematics.

In contrast, measured quadrupole spectrum properties suggest hadronization from a cold boosted source, possibly an expanding cylindrical shell. There is no correspondence with the sharp transition in jet properties observed near 50% fractional cross section, suggesting that the quadrupole phenomenon is not related to jet formation through a dense QCD medium. The narrow fixed boost distribution independent of A-A centrality appears to be incompatible with a Hubble scenario that would describe explosive expansion of a bulk medium, the mean boost increasing with A-A centrality [18].

XIII. SUMMARY

We have obtained azimuth quadrupole component $v_2\{2D\}$ data from transverse-rapidity y_t-differential correlations for 62- and 200-GeV Au-Au collisions. Application of novel analysis methods to 2D angular correlations permits accurate isolation of a nonjet (NJ) quadrupole component with simple systematic properties on y_t, Au-Au centrality, and collision energy.

Conventional v_2 analysis is based on nongraphical numerical methods (NGNMs) equivalent to fitting 1D azimuth correlations projected from some pseudorapidity η acceptance with a single cosine function. In the present analysis fits with a multielement fit model are applied to 2D angular correlations. The fit model is based on identification of certain geometric features in the 2D data without assumptions about physical mechanisms. In p-p and more-peripheral Au-Au collisions the data features are then characterized as jet-related or NJ by comparisons with theory. Those designations are maintained to central Au-Au collisions, although some physical interpretations may be questioned in more-central collisions.

In this analysis we have identified significant "nonflow" bias in published $v_2\{\text{method}\}(y_t,b)$ data, the bias derived mainly from a jet-related SS 2D peak. The bias is accurately predicted by separately measured SS peak properties. A variety of strategies has been developed previously in attempts to reduce the nonflow (jet) bias in conventional v_2 data, but the results are inconclusive.

The systematics of y_t-differential $v_2\{2D\}(y_t,b,\sqrt{s_{NN}})$ data from the present study and published y_t-integral $v_2\{2D\}(b,\sqrt{s_{NN}})$ data reveal that the quadrupole power-spectrum amplitude $V_2^2\{2D\}(y_t,b,\sqrt{s_{NN}})$ derived from those data is fully factorizable. The separate factors on rapidity, centrality, and energy are represented by simple functional forms. In terms of per-particle quadrupole measure $A_Q = \rho_0 v_2^2$ (ρ_0 is the single-particle density), the energy dependence is observed to be proportional to $\log(s/s_0)$ ($\sqrt{s_0} \approx 13$ GeV), as expected for a QCD process. The centrality dependence is essentially Gaussian on relative impact parameter b/b_0. The quadrupole power-spectrum centrality trend is $V_2^2\{2D\}(b,\sqrt{s_{NN}}) \propto N_{\text{part}} N_{\text{bin}} \epsilon_{\text{opt}}^2(b)$. The same trends accurately describe data from p-p to midcentral Au-Au collisions. A nonzero v_2 value for p-p collisions derived by extrapolation is consistent with a theory prediction based on an alternative (nonflow) QCD mechanism for the NJ quadrupole.

From the y_t-dependence factor *quadrupole spectra* can be reconstructed and a quadrupole *source boost* inferred for each collision system. The quadrupole spectrum shape is the same for three hadron species and for all collision systems, and the quadrupole source boost (a single value) is approximately independent of Au-Au centrality.

Our results have implications for hydrodynamic interpretations of A-A collisions. The universal quadrupole centrality trend can be contrasted with the trends for jet-related correlations which exhibit a common sharp transition within a small centrality interval, from N-N linear superposition in more-peripheral Au-Au collisions to a substantially different dependence in more-central collisions. In contrast, the trend for $v_2\{2D\}/\epsilon_{\text{opt}}$ remains smooth and slowly varying from p-p to more-central Au-Au collisions. If jet production responds to formation of or changes in a dense bulk medium, the azimuth quadrupole appears unresponsive to such a medium.

Further implications for hydro models arise from quadrupole spectrum results and quadrupole source-boost trends. The mean source boost does not vary significantly with Au-Au centrality, and the narrow boost distribution is inconsistent with Hubble flow of an expanding bulk medium. The NJ quadrupole amplitude *and* ratio $v_2\{2D\}/\epsilon$ fall to zero for most-central Au-Au collisions.

ACKNOWLEDGMENTS

This material is based upon work supported by the U.S. Department of Energy Office of Science, Office of Nuclear Physics under Award No. DE-FG02-97ER41020.

[1] J. Y. Ollitrault, Phys. Rev. D **46**, 229 (1992).
[2] D. Teaney, J. Lauret, and E. V. Shuryak, Phys. Rev. Lett. **86**, 4783 (2001).
[3] P. Huovinen and P. V. Ruuskanen, Annu. Rev. Nucl. Part. Sci. **56**, 163 (2006).
[4] P. F. Kolb, U. W. Heinz, P. Huovinen, K. J. Eskola, and K. Tuominen, Nucl. Phys. A **696**, 197 (2001).
[5] T. Hirano and M. Gyulassy, Nucl. Phys. A **769**, 71 (2006).
[6] L. P. Csernai, J. I. Kapusta, and L. D. McLerran, Phys. Rev. Lett. **97**, 152303 (2006).
[7] J. Adams *et al.* (STAR Collaboration), Nucl. Phys. A **757**, 102 (2005).
[8] A. M. Poskanzer and S. A. Voloshin, Phys. Rev. C **58**, 1671 (1998).
[9] J. Adams *et al.* (STAR Collaboration), Phys. Rev. C **72**, 014904 (2005).
[10] J. Adams *et al.* (STAR Collaboration), Phys. Rev. C **73**, 064907 (2006).
[11] J. Adams *et al.* (STAR Collaboration), J. Phys. G **32**, L37 (2006).

[12] J. Adams *et al.* (STAR Collaboration), J. Phys. G **34**, 451 (2007).
[13] T. A. Trainor and D. T. Kettler, Phys. Rev. D **74**, 034012 (2006).
[14] T. A. Trainor, D. T. Kettler, D. J. Prindle, and R. L. Ray, J. Phys. G **42**, 025102 (2015).
[15] D. T. Kettler (STAR Collaboration), Eur. Phys. J. C **62**, 175 (2009).
[16] G. Agakishiev *et al.* (STAR Collaboration), Phys. Rev. C **86**, 064902 (2012).
[17] D. Kettler (STAR Collaboration), J. Phys. Conf. Ser. **270**, 012058 (2011).
[18] T. A. Trainor, Phys. Rev. C **78**, 064908 (2008).
[19] T. A. Trainor and D. J. Prindle, Phys. Rev. D **88**, 094018 (2013).
[20] T. A. Trainor, arXiv:1407.6422.
[21] R. J. Porter and T. A. Trainor (STAR Collaboration), J. Phys. Conf. Ser. **27**, 98 (2005).
[22] R. J. Porter and T. A. Trainor (STAR Collaboration), PoS **CFRNC2006**, 004 (2006).
[23] T. A. Trainor, R. J. Porter, and D. J. Prindle, J. Phys. G **31**, 809 (2005).
[24] J. Adams *et al.* (STAR Collaboration), Phys. Lett. B **634**, 347 (2006).
[25] K. H. Ackermann *et al.* (STAR Collaboration), Nucl. Instrum. Methods Phys. Res., Sect. A **499**, 624 (2003).
[26] T. A. Trainor and D. T. Kettler, Int. J. Mod. Phys. E **17**, 1219 (2008).
[27] T. Sjöstrand and M. van Zijl, Phys. Rev. D **36**, 2019 (1987).
[28] X.-N. Wang and M. Gyulassy, Phys. Rev. D **44**, 3501 (1991); version 1.382.
[29] T. A. Trainor and D. T. Kettler, Phys. Rev. C **83**, 034903 (2011).
[30] B. Alver and G. Roland, Phys. Rev. C **81**, 054905 (2010).
[31] M. Luzum, Phys. Lett. B **696**, 499 (2011).
[32] T. A. Trainor, J. Phys. G **40**, 055104 (2013).
[33] T. A. Trainor, Mod. Phys. Lett. A **23**, 569 (2008).
[34] D. Kharzeev and M. Nardi, Phys. Lett. B **507**, 121 (2001).
[35] T. A. Trainor and D. J. Prindle, arXiv:hep-ph/0411217.
[36] C. L. Phillips, J. M. Parr, and E. A. Riskin, *Signals, Systems and Transforms* (Prentice Hall, Upper Saddle River, NJ, 2007).
[37] M. B. De Kock, H. C. Eggers, and T. A. Trainor, arXiv:1502.04475.
[38] J. Adams *et al.* (STAR Collaboration), Phys. Rev. Lett. **95**, 152301 (2005).
[39] B. I. Abelev *et al.* (STAR Collaboration), Phys. Rev. C **80**, 064912 (2009).
[40] T. A. Trainor, Phys. Rev. C **81**, 014905 (2010).
[41] B. I. Abelev *et al.* (STAR Collaboration), Phys. Rev. C **79**, 034909 (2009).
[42] F. Cooper and G. Frye, Phys. Rev. D **10**, 186 (1974).
[43] B. I. Abelev *et al.* (STAR Collaboration), Phys. Rev. C **77**, 054901 (2008).
[44] C. Adler *et al.* (STAR Collaboration), Phys. Rev. C **66**, 034904 (2002).
[45] J. Adams *et al.* (STAR Collaboration), Phys. Rev. Lett. **92**, 052302 (2004).
[46] T. A. Trainor, Int. J. Mod. Phys. E **17**, 1499 (2008).
[47] N. Borghini, P. M. Dinh, and J.-Y. Ollitrault, Phys. Rev. C **63**, 054906 (2001).
[48] K. Aamodt *et al.* (ALICE Collaboration), Phys. Rev. Lett. **105**, 252302 (2010).
[49] S. A. Voloshin (STAR Collaboration), AIP Conf. Proc. **870**, 691 (2006).
[50] A. M. Poskanzer *et al.* (NA49 Collaboration), Nucl. Phys. A **661**, 341 (1999).
[51] T. A. Trainor and D. T. Kettler, Phys. Rev. C **84**, 024910 (2011).
[52] S. A. Voloshin and A. M. Poskanzer, Phys. Lett. B **474**, 27 (2000).
[53] B. Z. Kopeliovich, A. H. Rezaeian, and I. Schmidt, Phys. Rev. D **78**, 114009 (2008).